(12)

AD A116796

Combustion Processes in
Solid Propellant Cracks

by
K. K. Kuo
M. Kumar
S. M. Kovacic
J. E. Wills
T. Y. Chang
Pennsylvania State University
for the
Research Department

JUNE 1981

**NAVAL WEAPONS CENTER
CHINA LAKE, CALIFORNIA 93555**

DTIC
ELECTE
JUL 1 2 1982
S   D

B

DTIC FILE COPY

82 07 12 027

Naval Weapons Center
AN ACTIVITY OF THE NAVAL MATERIAL COMMAND

FOREWORD

This is the final report for a research program conducted by
Pennsylvania State University in support of the Aerothermochemistry
Division's studies of combustion processes in solid propellant cracks.
Continuing support from Naval Weapons Center covered a period from
1 February 1978 to 31 January 1980.

This report was reviewed for technical accuracy by Channon F.
Price of the Aerothermochemistry Division. Work was supported by Naval
Weapons Center under Contract N60530-78-C0069. This report is a continu-
ation of the research program on "Transient Combustion Processes in
Solid Propellant Cracks," carried out in the Mechanical Engineering
Department of the Pennsylvania State University.

This report is released at the working level. Because of the
continuing nature of this research, changes may be made in the future.

Approved by   Under authority of
E. B. ROYCE, *Head*   W. B. HAFF
Research Department   CAPT, U.S. Navy
11 June 1981   *Commander*

Released for publication by
R. M. HILLYER
Technical Director

REPORT DOCUMENTATION PAGE		READ INSTRUCTIONS BEFORE COMPLETING FORM
1. REPORT NUMBER NWC TP 6278	2. GOVT ACCESSION NO. AD-A116796	3. RECIPIENT'S CATALOG NUMBER
4. TITLE (and Subtitle) COMBUSTION PROCESSES IN SOLID PROPELLANT CRACKS		5. TYPE OF REPORT & PERIOD COVERED FINAL 1 Feb 1978 – 31 Jan 1980
		6. PERFORMING ORG. REPORT NUMBER NWC TP 6278
7. AUTHOR(s) K. K. KUO, M. KUMAR, S. M. KOVACIC, J. E. WILLS, T. Y. CHANG		8. CONTRACT OR GRANT NUMBER(s) N60530–78–C–0069
9. PERFORMING ORGANIZATION NAME AND ADDRESS PENNSYLVANIA STATE UNIVERSITY UNIVERSITY PARK, PENNSYLVANIA 16802		10. PROGRAM ELEMENT, PROJECT, TASK AREA & WORK UNIT NUMBERS B0003–SB
11. CONTROLLING OFFICE NAME AND ADDRESS NAVAL WEAPONS CENTER CHINA LAKE, CALIFORNIA 93555		12. REPORT DATE JUNE 1981
		13. NUMBER OF PAGES 98
14. MONITORING AGENCY NAME & ADDRESS(If different from Controlling Office)		15. SECURITY CLASS. (of this report) UNCLASSIFIED
		15a. DECLASSIFICATION DOWNGRADING SCHEDULE
16. DISTRIBUTION STATEMENT (of this Report) APPROVED FOR PUBLIC RELEASE; DISTRIBUTION UNLIMITED		
17. DISTRIBUTION STATEMENT (of the abstract entered in Block 20, if different from Report)		
18. SUPPLEMENTARY NOTES		
19. KEY WORDS (Continue on reverse side if necessary and identify by block number) SOLID PROPELLANT DEFLAGRATION–TO–DETONATION TRANSITION CONVECTIVE BURNING		
20. ABSTRACT (Continue on reverse side if necessary and identify by block number) (SEE BACK OF FORM)		

DD FORM 1473 1 JAN 73

EDITION OF 1 NOV 65 IS OBSOLETE
S/N 0102-014-6601

(U) *Combustion Processes in Solid Propellant Cracks,* by
K. K. Kuo, M. Kumar, S. M. Kovacic, J. E. Wills, and
T. Y. Chang, Pennsylvania State University, University Park,
Pennsylvania. China Lake, California, Naval Weapons Center,
June 1981, 98 pp. (NWC TP 6278, Publication UNCLASSIFIED.)

(U) This report presents results of a study of combustion
processes in solid propellant cracks. As might be expected,
under moderate chamber pressurization rates ($<10^4$ atm/s), the
theoretical predictions, as well as the experimental observations,
indicate that the ignition front propagates from the entrance
of the crack to the tip. However, under rapid chamber pressurization
rates (10^5 atm/s or higher), the tip region of the crack was
observed to ignite before the arrival of the convective
ignition front. (Ignition is defined here as the onset of
emission of luminous light from the propellant surface with
some material loss. A theoretical model has been developed
to explain the tip ignition phenomena. The model considers:
a one-dimensional transient heat conduction equation for the
solid phase, and one-dimensional, unsteady mass and energy
conservation equations for the gas phase near the crack tip.
Both experimental and theoretical results indicate that the
ignition delay time decreases as the pressurization rate is
increased. Theoretically calculated ignition delay times are
in good agreement with the experimental data. Based upon
this agreement, ignition near the crack-tip region is
considered to be caused by the enhanced turbulent transport
of energy in the gas phase, which is driven by strong
compression waves.

(U) The Crack Combustion Code (CCC) has been combined
with the consolidated Nonlinear Finite-Element Analysis
Program (NFAP). Initial runs of the combined program
(CCC/NFAP) indicate that the structural deformation and
combustion phenomena are interrelated. The combustion
phenomena inside the crack may either enhance or retard,
depending upon the effect of mechanical deformation on the
gap width along the crack. The program has the option of
using either the linear elastic or linear viscoelastic material
model. As expected, results show that the viscoelastic model
is more realistic for the solid propellant.

(U) Test firings were conducted to determine the one-
dimensionality of the flame front. It was observed that,
except near the entrance region, the one-dimensional
assumption for the flame propagation is quite appropriate.
Experiments were continued to determine the effect of
propellant crack geometry on flame propagation inside a
crack.

(U) A complete set of dimensionless parameters which
govern the flame-spreading and combustion phenomena inside
a solid propellant crack were obtained.

CONTENTS

INTRODUCTION

A very important characteristic of a gas permeable solid propellant is that it undergoes the transition from normal burning to detonation under certain operating conditions. A transition from deflagration-to-detonation (DDT) may not only cause malfunction or failure of a solid propellant motor, but it is also a potential source of hazard. DDT usually involves very high flame propagation rates, high pressures, and large burning surface areas. DDT is therefore more likely to occur in gas permeable propellants, such as granular propellant beds or propellant grains with flaws or cracks which have large burning surface areas.

Cracks inside solid propellant grains, which are likely to be encountered in high-energy propellants with high-solids loading, can allow hot, high pressure gases to penetrate the cavity. The combustion processes inside the crack can produce much higher pressure than the designed maximum operating pressure. If the local pressure rise due to the gasification is sufficiently rapid, it may produce strong compression waves, or even shock waves which can initiate detonation. Furthermore, for DDT in damaged propellant grains with cracks, crack branching/propagation must take place to provide the additional surface area. Some experimental and theoretical studies, based purely on solid mechanics considerations, have been conducted to predict crack propagation in solid propellant grains. However, realistic predictions of accelerative convective burning and crack propagation cannot be made unless a combustion program incorporating a structural analysis program is used.

Convective burning, however, is not the only mechanism responsible for producing the steep pressure gradients that lead to the transition to detonation. There are other mechanisms which may also be important in DDT processes. The presence of numerous ignited spots and ablating surfaces at some distance from the combustion zone in a damaged propellant may enhance the possibility of DDT. For example, ignited spots can be produced by reflection of shock-like compression waves at the propellant surface located in the region ahead of the combustion zone. A similar phenomenon was observed during the course of experimental investigations of ignition and flame-spreading inside a solid propellant crack. As noted in our last annual report,[1] under rapid pressurization

---

[1]Naval Weapons Center. *Convective Burning in Isolated Solid Propellant Cracks*, by K. K. Kuo, R. L. Kovalcin, and S. J. Ackman. China Lake, Calif., NWC, February 1979. (NWC TP 6049, publication UNCLASSIFIED.)

rates ($\sim 10^5$ atm/s), anamolous ignition was observed near the crack-tip region. High-speed ($\sim 15{,}000$ pps) motion picture films used to record the experimental observations of the flame propagation inside the crack show that, at high chamber pressurizaton rates, the tip region of the crack ignites before the convective ignition front propagates from the crack entrance to the tip. Consequently, under these operating conditions, two flame fronts moving in opposite directions have been observed: one propagates from the crack entrance and the other from the crack tip.

The observed ignition phenomena near the tip region could be one of the very important mechanisms responsible for the generation of ignited spots in a region ahead of the combustion zone. Indeed, these ignited spots can contribute significantly to the DDT process. These studies in convective burning and related topics are essential for a sound physical understanding of the phenomena involved in the DDT process. Moreover, solid knowledge of the ignition phenomena associated with strong convective burning is an important step towards the goal of modeling a more complex DDT phenomenon. The main objectives of the work performed during this reporting period are as follows.

1. To identify the possible mechanism for ignition near the crack tip region, and to develop an analytical model for its prediction.

2. To consolidate the Nonlinear Finite-Element Analysis Program (NFAP) and combine it with the Crack Combustion Code (CCC).

3. To experimentally verify the one-dimensional assumption of the flame front.

4. To determine a complete set of dimensionless parameters that govern the combustion phenomena inside a solid propellant crack, for the combined problem of aerothermochemistry and solid mechanics.

5. To continue experimental firings of single pore propellants with narrow gap-widths, for the purpose of establishing a data base and for further verification of the theoretical model.

BACKGROUND

A considerable amount of work in the area of solid propellant crack combustion has been conducted at the Pennsylvania State University.[1-3] Substantial progress has been made in both experimental and

[2]K. K. Kuo, A. T. Chen, and T. R. Davis. "Convective Burning in Solid-Propellant Cracks," *AIAA Journal*, Vol. 16, No. 6 (June 1978), pp. 600-607.

[3]Naval Weapons Center. *Transient Combustion in Solid Propellant Cracks*, by K. K. Kuo, D. R. McClure, A. T. Chen, and F. C. Lucas. China Lake, Calif., NWC, October 1977. (NWC TP 5943, publication UNCLASSIFIED.)

theoretical areas towards a better understanding of the convective burning inside a solid propellant crack. Some of the important achievements are as follows:

1.   A quasi-one-dimensional theoretical model has been developed to describe the transient combustion processes in a propellant crack. The theoretical model can be used to predict the flame propagation, pressurization, and gas dynamic phenomena at various locations along the propellant cavity.

2.   A computer program, based upon the above theoretical model, has been developed and successfully implemented. This program can be used to predict the flame propagation and combustion phenomena inside the propellant crack.

3.   A laboratory-sized combustion chamber, utilizing current techniques in high-speed photography and pressure recording, has been developed for solid propellant crack combustion experiments and model validation.

4.   In order to simulate the conventional pressurization rates during rocket motor ignition transients, a reproducible solid propellant ignition system has been designed and fabricated.

5.   Experimental firings with single-pore propellant grain have been conducted to study the effects of crack geometry, chamber pressurization rates, propellant type, etc., on flame spreading and pressure variation inside the cavity.

6.   The combustion program has been modified to consider different ignition criteria, and to obtain the indepth temperature profile of the solid propellant, in order that the dynamic burning behavior can be studied.

7.   An extensive literature survey on the combustion phenomena inside a solid propellant crack, and its relevance to the process of DDT, has been conducted.

THEORETICAL WORK

MODELING OF THE CRACK TIP IGNITION PHENOMENA

Introduction

As mentioned earlier, under rapid chamber pressurization conditions ignition may be achieved near the crack tip region--far ahead of the convective combustion zone in an isolated crack. It is conceivable that

5

in the combustion of a prefractured or granulated propellant, numerous ignited regions can be generated in a similar manner by rapid rates of gasification and pressurization in the combustion zone. These ignited regions can propagate further to produce even higher gasification rates in the combustion chamber, or in an actual rocket motor. Flame-front propagation rates can be increased not only by the presence of these ignited regions, but also by the steepening of compression or shock waves near the flame front; eventually, the waves become strong enough to initiate a final transition to detonation. Therefore, a fundamental understanding of the basic mechanisms that contribute to the generation of these ignited regions would be an important step in the convective burning and DDT study.

The observed ignition of the tip region of the crack before the arrival of the convective ignition front may have been caused by one or more of the following mechanisms:

1.   Turbulent diffusion of the hot product gases to the crack tip region, and the stagnation heating of the propellant by the hot gases at the crack tip.

2.   Compression/shock wave heating of the gas adjacent to the propellant surface and the stagnation heating of the propellant by the hot gases at the crack tip.

3.   Local heat release, due to the chemical reaction of the combustible species transported to the crack tip by the initial pressure gradient.

4.   Radiative heating of the crack tip.

5.   Vaporization of the fuel binder at low temperatures, followed by a gas phase reaction between the fuel and the oxidizer gases in the air near the crack tip region.

Ignition near the tip region can be achieved if some of the combustible species evaporate from the propellant surface near the entrance of the crack and if these species are transported by the initial pressure gradient to the crack-tip region, where they react and ignite. Under these circumstances, it is possible to observe the ignition of the tip region prior to the arrival of the convective ignition front. In order to investigate this possibility, an inert crack was formed with propellant only at the tip. Tests conducted with this type of inert crack also showed ignition at the tip, thus eliminating the third mechanism noted above.

Some preliminary calculations were conducted to evaluate the effect of radiative heating. Calculations showed that radiative heating of the propellant at the tip by the hot gases in the combustion chamber is far

too low to cause ignition. One of the main reasons for such a small amount of radiative heating is that the crack length to hydraulic diameter ratio is on the order of 80, resulting in a very small shape factor. Therefore, the fourth mechanism mentioned above was eliminated.

The fifth mechanism, i.e., the gas phase reaction mechanism is quite probable for propellants using fuel with low vaporization temperatures. However, the gas phase reaction may not be very appreciable for propellants with fuel binders having high vaporization temperatures (i.e., of the same order as the vaporization temperature of the oxidizer crystals). Propellant A, for which all tip ignition experiments were conducted, is an example of the latter type; in other words, its fuel-binder and oxidizer have almost identical vaporization temperatures. For the present study, therefore, the gas phase ignition mechanism may not be significant, and, hence, can be neglected. It should be noted, however, that for other types of propellants this mechanism may be important.

This leaves us with only two possible mechanisms that should be considered. The ignition could be caused by a combination of these two mechanisms. An extensive literature survey was conducted for these two heating mechanisms. The heat transfer mechanism near the closed end of a long isolated pore, with a time-varying interface temperature, has not been studied in the past. Some of the published results which are related to the problem being considered are discussed in the following paragraphs.

McAlevy, Cowan and Summerfield[4,5] studied the mechanism of ignition of composite solid propellants by hot gases in a shock tube. The objectives of their study were to measure the ignition delays of test propellants heated to a shock; to develop a theoretical model based upon the gas phase ignition mechanism in order to calculate the ignition delay; and to study the effect of oxygen concentration on the ignition delay. For the experimental measurements, the specimen was flush-mounted in the end wall of a shock tube. The propellant was heated by high temperature, high pressure, stagnant gas behind the reflected shock wave. Photocells were used to detect ignition. In the theoretical model, it was assumed that at the instant of shock reflection a stagnant column of hot gases comes in contact with the propellant surface. The temperature of this column of gas was obtained from the reflected shock relationships. The interface temperature, which remains constant with time,

[4]R. F. McAlevy, III, P. L. Cowan, and M. Summerfield. "The Mechanism of Ignition of Composite Solid Propellants," *Solid Propellant Rocket Research*. Volume 1, Progress in Astronautics and Rocketry, an American Rocket Society series. New York, Academic Press, 1960, pp. 673-692.

[5]R. F. McAlevy, III. "The Ignition Mechanism of Composite Solid Propellants," Ph.D. Thesis, Princeton University. June 1960.

was obtained by considering two uniform temperature, semi-infinite bodies brought in contact at the instant of shock reflection. Pyrolized fuel vapor generated at the propellant surface propagates upstream at a rate governed by the laws of mass diffusion. This fuel vapor reacts with the gaseous oxygen and ignition takes place as a result.

The general conclusions of McAlevy, Cowan, and Summerfield were that the observed ignition delay is the time required for sufficient fuel to react with the gaseous oxygen, and that the ignition delay time was found to increase with the decrease in oxygen concentration and pressure. Since this was the first study on the gas phase ignition model, the analytic model has several limitations. The assumption of constant propellant surface temperature condition is not very realistic. Calculated ignition delay time based on their model was an order of magnitude higher than the experimentally observed ignition delay. Contrary to their theoretical predictions, they observed a longer (two times) ignition delay for pure fuel than for composite propellant with the same fuel.

Hermance, Shinnar, and Summerfield improved the gas phase ignition model by including oxidizer species equations.[6] Later, they proposed a more realistic model for pure fuel, which included the effect of heat feedback to the propellant surface. Unfortunately, they did not make comparisons with the experimental data and, therefore, no conclusions about the quantitative prediction capabilities can be drawn. Although the effect of oxygen concentration (as observed by McAlevy et al.) supports the concept of gas phase ignition, there remains a large number of uncertainties and unknowns which could strongly influence the quantitative predictions of ignition delay. Some of these are: detailed processes involved in fuel and oxidizer pyrolysis; gasification temperatures of various ingredients in the propellant; the effect of exothermic oxidation at the propellant surface; and the catalytic effect of oxidizer gases on the vaporizing propellant surface. Because of these reasons and the fact that the studies were conducted for shock tube conditions where the effect of pressurization rates cannot be observed, the results of the gas phase ignition model cannot be used for the present study.

---

[6]C. E. Hermance, R. Shinnar, and M. Summerfield. "Ignition of Hot, Stagnant Gas Containing an Oxidizer," *AIAA J.*, Vol. 3, No. 9 (September 1965), pp. 1584-1592.

[7]------. Ignition of an Evaporating Fuel in a Hot Oxidizing Gas, Including the Effect of Heat Feedback," *Astronautica Acta*, Vol. 12, No. 2 (March-April 1966), pp. 95-112.

Fay and Kemp predicted the heat transfer rates to the end wall of a shock tube.[8] In their analysis, the end wall of a shock tube was assumed to be suddenly put in contact with the quiescent hot gas. The pressure of the gas behind the reflected shock was determined from shock relationships. Continuity and energy equations in the gas phase were used. The wall was assumed to remain at its initial temperature. By using an integral method, a similarity type of solution was obtained for the heat transfer rate to the end wall. A closed form solution was obtained, which predicted the heat flux as a function of shock velocity and time. For the following reasons, results obtained from the study cannot be used to predict the heat transfer rate in the present study: a shock tube type of study cannot take into account the effect of pressurization rates; the end-wall temperature is assumed to be at its initial constant temperature, and, therefore, is not realistic for ignition studies; and, the rate of heat transfer to the end wall can only decrease with time ($\dot{q}_w \sim 1/\sqrt{t}$) in the analysis (this is true for the Fay-Kemp study, but is contrary to the physical situation of the present investigation).

Levy and Potter made some transient measurement in a rarefaction wave tube.[9] Their objectives were to build and calibrate a heat transfer instrument, to perform transient heat flux measurements in a rarefaction wave tube, and to evaluate the significant parameters which influence the instrument performance in the measurement of the transient heat flux. Using a heat transfer measuring instrument, they experimentally measured the heat transfer from the end wall for various pressure ratios. In their theoretical approach, they used energy and continuity equations in a control volume very close to the end wall. Temperature of the end wall was assumed to be constant, and the gas temperature variation was assumed to be a second order polynomial of the distance from the end wall. The expansion process was assumed to be isentropic. From their analysis, they found that $\dot{q}_w / \sqrt{P_{initial}/P_{atm}}$ was a function of a dimensionless time $tc_{initial}/L_{tube}$. This analysis has very limited use for the present study because of the severe simplifying assumptions and the physical process of depressurization.

---

[8] J. A. Fay and N. H. Kemp. "Theory of Heat Transfer to a Shock-Tube End-Wall from an Ionized Monatomic Gas," *J. Fluid Mech.*, Vol. 21 (1965), pp. 659-672.

[9] M. J. Levy and J. H. Potter. "Some Transient Measurement in a Rarefaction Wave Tube," *J. of Engineering for Industry*, Trans. ASME, Series B, Vol. 86, November 1964, pp. 365-370.

Chao gave an alternative approach[10] to the same problem solved by Levy and Potter. Using an analytic solution, Chao solved the energy and continuity equations for an ideal gas. The end wall was assumed to remain at its initial temperature. Gas density was assumed to be independent of the axial location. By using a coordinate transformation, the energy equation for the gas phase was converted into the form of a heat equation. A closed form solution for the dimensionless heat flux was obtained. The predicted heat transfer rate was in close agreement with Levy and Potter's data. Once again, the assumption of constant end wall temperature and the physical process of depressurization makes this analysis of very limited use to the present study.

Theoretical Model

From the above literature survey, it is clear that none of the existing theoretical models can be employed to study the current ignition phenomenon observed. Therefore, a theoretical model was developed to predict the ignition delay and its dependence on the pressurization rate. The theoretical model considers an inert crack--a rectangular shaped inert channel with propellant only at the tip. When the chamber is pressurized, hot ignition gases penetrate the cavity and are reflected from the solid propellant at the closed end. Ignition delay is defined as the time lag between the arrival of the pressure front at the tip and the incipient ignition.

As soon as the hot gases reach the closed end of the crack, heat starts to flow into the propellant surface and, consequently, the surface temperature rises. Ignition is defined as the attainment of a critical temperature at the propellant surface. It is assumed that the solid or gas phase reaction takes place before the onset of ignition. Here, the tacit assumption is made that there is little time between the attainment of a critical surface temperature and the reaction between the fuel and the oxidizer species to cause ignition. For propellant A, the ignition of which is studied here, the surface temperature ignition criteria may be quite suitable since its fuel binders and the oxidizer have an almost identical vaporization temperature. It should be pointed out that if the fuel vaporization temperature is much lower than that of the oxidizer crystals, the gas phase reaction between vaporized fuel and oxidizer in the ambient gas may be important, and that this ignition criteria may not be valid.

---

[10]B. T. Chao. "End-Wall Heat Transfer in a Rarefaction Wave Tube," *J. Heat Transfer*, August 1965, pp. 349-352.

In the theoretical model, the propellant is considered to be a one-dimensional, semi-infinite solid which is brought in contact with hot gases at the instant of the arrival of the pressure front at the tip. The hot gases cause heat transfer to the propellant surface. A schematic diagram of the physical model considered is given in Figure 1.
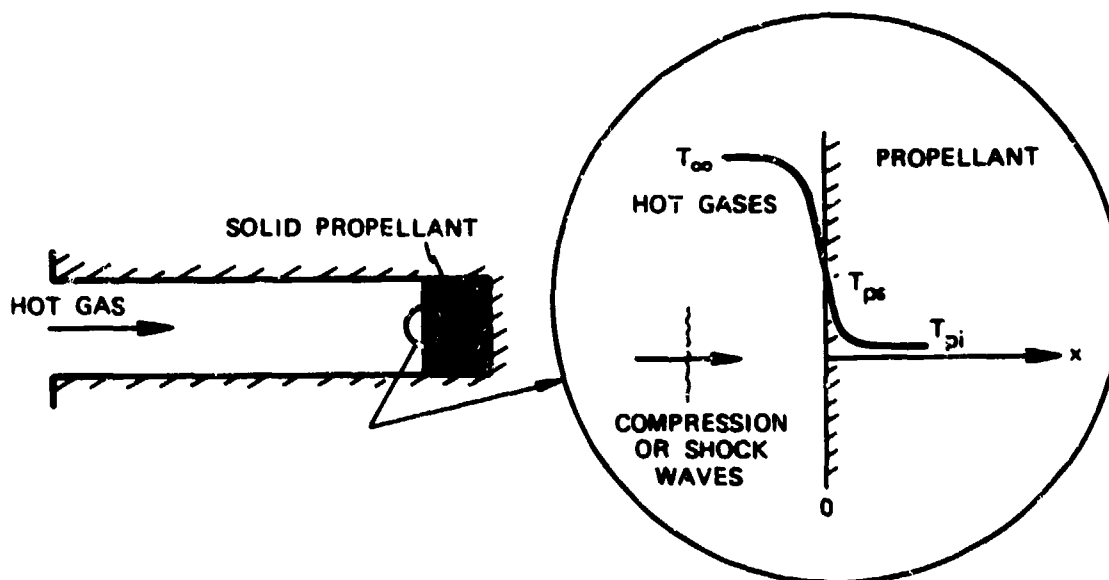
FIGURE 1. Schematic Diagram of the Physical Model for the Tip Ignition Study.

The solid phase heat conduction equation is:

$$\frac{\partial T_p}{\partial t} = \alpha_p \frac{\partial^2 T_p}{\partial x^2} \tag{1}$$

The initial and boundary conditions are:

$$t = 0: \quad T_p(o,x) \quad T_{pi}$$

$$x = \infty: \quad T_p(t,\infty) = T_{pi} \tag{2}$$

$$x = 0: \quad k_p \frac{\partial T_p}{\partial x}(t,0^+) = k \frac{\partial T}{\partial x}(t,0^-) = -\dot{q}_w(t)$$

11

where $\dot{q}_w(t)$ is the rate of heat transfer from the hot gases to the propellant surface and is unknown. In order to determine the heat flux at the propellant surface, the gas phase equations have to be considered.

Assuming the bulk flow to be predominantly one-dimensional, the transient mass and energy conservation equations are considered for the gas phase. Experimentally obtained pressure-time trace near the crack tip region is used, instead of solving the pressure at the crack tip through the use of momentum equation. The region of interest is that adjacent to the solid propellant surface. The governing equations can be written as follows:

Continuity equation:

$$\frac{\partial \rho}{\partial t} + \frac{\partial \rho u}{\partial x} = 0 \tag{3}$$

Energy equation:

$$\frac{\partial (\rho h)}{\partial t} + \frac{\partial (\rho u h)}{\partial x} - \frac{\partial P}{\partial t} - \overset{\text{small}}{u \frac{\partial P}{\partial x}} = \frac{\partial}{\partial x}\left(k \frac{\partial T}{\partial x}\right) + \overset{\text{small}}{\underset{\text{dissipation}}{\phi}} \tag{4}$$

$$P(t,0^-) = P_{measured}(t) \tag{5}$$

In order to simplify the analysis, the following basic assumptions are made:

1. $u \frac{\partial P}{\partial x} \ll \frac{\partial P}{\partial t}$ for the region of interest, i.e., locally uniform pressure near the propellant surface.

2. The viscous dissipation, ϕ, is small.

3. The specific heat, C_p, is constant.

4. The hot gases behave as ideal gas.

Using these assumptions and then taking the Favre Average[11] of the gas phase conservation Eq. (3) and (4), we get (Appendix A summarizes the basic definitions and operation rules for Favre Averaging):

---

[11]A. Favre. "Equations des Gaz Turbulents Compressibles," *J. de Mechanique*, Vol. 4, No. 3 (1965), pp. 361-390.

$$\frac{\partial \rho}{\partial t} + \frac{\partial}{\partial x}(\overline{\rho}\tilde{u}) = 0 \tag{6}$$

$$\overline{\rho}\frac{\partial \tilde{h}}{\partial T} + \overline{\rho}\tilde{u}\frac{\partial \tilde{h}}{\partial x} - \frac{\partial \overline{P}}{\partial t} = \frac{\partial}{\partial x}(\frac{\mu}{Pr}\frac{\partial \tilde{h}}{\partial x}) + \frac{\partial}{\partial x}(k\frac{\partial \overline{T''}}{\partial x} - \overline{\rho h''u''}) \tag{7}$$

Considering $k\frac{\partial \overline{T''}}{\partial x}$ to be negligible in comparison with $\overline{\rho h''u''}$ and defining

$$-\overline{\rho h''u''} \equiv \frac{\mu_t}{Pr_t}\frac{\partial \tilde{h}}{\partial x} \tag{8}$$

The energy equation can be written in the following form:

$$\overline{\rho}\frac{\partial \tilde{h}}{\partial r} + \overline{\rho}\tilde{u}\frac{\partial \tilde{h}}{\partial x} - \frac{\partial \overline{P}}{\partial t} = \frac{\partial}{\partial x}\left(\frac{\mu}{Pr}\frac{\partial \tilde{h}}{\partial x} + \frac{\mu_t}{Pr_t}\frac{\partial \tilde{h}}{\partial x}\right) \tag{9}$$

The initial and boundary conditions are

I.C. $t = 0$ $\tilde{T}(0,x) = T_i$

B.C.1 $x = -\infty$ $\tilde{T}(t,-\infty) = T_\infty$

B.C.2 $x = 0$ $\tilde{T}(t,0) = T_p(t,0)$ (10)

Solution Method

Integrating the continuity equation (Eq. (6)) and using the boundary condition, at

$$x = 0 \quad \tilde{u} = 0$$

we get

$$\overline{\rho}\tilde{u} = \int_0^x -(\partial \overline{\rho}/\partial t)dx \tag{11}$$

Replacing the $\overline{\rho}\tilde{u}$ term in the gas phase energy equation (Eq. (9)) by Eq. (11), we get:

$$\overline{\rho}\frac{\partial \tilde{h}}{\partial t} - \left[\int_c^x \frac{\partial \rho}{\partial t}dx\right]\frac{\partial \tilde{h}}{\partial x} - \frac{\partial \overline{P}}{\partial t} = \frac{\partial}{\partial x}\left(\frac{\mu}{Pr}\frac{\partial \tilde{h}}{\partial x} + \frac{\mu_t}{Pr_t}\frac{\partial \tilde{h}}{\partial x}\right) \tag{12}$$

Now, in order to obtain the heat flux to the propellant surface and the propellant surface temperature, Eq. (1) and (12), together with the boundary conditions (Eq. (2) and (10)) must be solved simultaneously. An attempt was made to solve these equations analytically to obtain closed form solutions for the propellant surface temperature. The

partial differential equations can be transformed, in the transformed coordinates, into a diffusion type of equation (see Appendix B). Some difficulties were encountered in obtaining analytical solution, as discussed in Appendix 2. In order to obtain theoretical results to compare with experimental data, this set of equations is solved numerically.

The region near the propellant surface is the most interesting; it is here that large temperature gradients exist. For mathematical tractability, the infinite x-region is transformed into a finite region, using transformation given below. The transformed coordinate system also makes possible a finer grid-size near the propellant surface in the real spatial coordinate, while using a uniform grid in the transformed coordinate.

For the gas phase region:

$$-\infty \leq x < 0$$

$$z = -[1 - 1/(1 - Ax)] \tag{13}$$

which gives

$$x = 0 \qquad z = 0$$

$$x = -\infty \qquad z = -1$$

$$\frac{\partial}{\partial x} = A(1 + z)^2 \frac{\partial}{\partial z}$$

$$\frac{\partial}{\partial x^2} = A^2(1 + z)^4 \frac{\partial^2}{\partial z^2} + 2A^2(1 + z)^3 \frac{\partial}{\partial z}$$

After making these substitutions into the gas phase energy equation (Eq. (12)) and the initial boundary conditions (Eq. (10)), and some simplification as well, we get

$$\frac{\partial \tilde{T}}{\partial t} = \left\{ \left[\int_0^z \frac{\partial \bar{\rho}}{\partial t} \frac{dz}{(1 + z)^2} \right] \frac{(1 + z)^2}{\bar{\rho}} + \frac{1}{\bar{\rho}} \left(\frac{\mu}{Pr} + \frac{\mu_t}{Pr_t} \right) 2A^2 \left(1 + z \right)^3 \right\} \frac{\partial \tilde{T}}{\partial z}$$

$$+ \left(\frac{\mu}{Pr} + \frac{\mu_t}{Pr_t} \right) \frac{1}{\bar{\rho}} A^2 \left(1 + z \right)^4 \frac{\partial^2 \tilde{T}}{\partial z^2} + \frac{1}{\bar{\rho} C_p} \frac{\partial \bar{P}}{\partial t} \tag{14}$$

I.C. $t = 0$ $\tilde{T}(0,z) = T_i$

B.C.1 $z = -1$ $\tilde{T}(t,-1) = T_\infty$

B.C.2 $z = 0$ $\tilde{T}(t,0) = T_p(t,0)$ (15)

The transformation for the solid phase region $0 \leq x \leq \infty$

$$Z = [1 - \frac{1}{1 + A_1 x}]$$ (16)

which gives

$x = 0$ $z = 0$

$x = \infty$ $z = 1$

$$\frac{\partial}{\partial x} = A_1 (1 - z)^2 \frac{\partial}{\partial z}$$

$$\frac{\partial^2}{\partial x^2} = A_1^2 (1 - z)^4 \frac{\partial^2}{\partial z^2} - 2A_1^2 (1 - z)^3 \frac{\partial}{\partial z}$$

After making these substitutions into Eq. (1) and (2), and after some simplifications, we get

$$\frac{\partial T_p}{\partial t} = \left[-2A_1^2 \left(1 - z\right)^3 \alpha_p \right] \frac{\partial T_p}{\partial z} + \left[A_1^2 \left(1 - z\right)^4 \alpha_p \right] \frac{\partial^2 T_p}{\partial z^2}$$ (17)

I.C. $t = 0$ $T_p(0,z) = T_{p_i}$

B.C.1 $z = 1$ $T_p(t,1) = T_{p_i}$

B.C.2 $z = 0$ $Ak \frac{\partial \tilde{T}}{\partial z} (t,0^-) = A_1 k_p \frac{\partial T_p}{\partial z} (t,0^+)$ (18)

Numerical Scheme

The coupled set of particl differential equations (namely, the energy equation for the fluid and the transient heat conduction equation for the propellant), was solved using a finite difference numerical technique. The most important solution parameter was the interfacial temperature as a function of time. The heat flux to the propellant surface was then easily computed from the calculated temperature distribution. The finite difference equation was written for the equations in

transformed coordinates. As mentioned in the previous section, this transformation made possible the use of uniform grid spacing in z-coordinate, thereby bypassing the instability associated with nonuniform grid spacing, which would have been necessary for the x-coordinate. The compression of the axis near the interface was controlled by the parameters A and A_1. Larger values of A and A_1 result in finer grid spacing near the interface.

The two partial differential equations (Eq. (14) and (17)), to be solved are of the form

$$\frac{\partial T}{\partial t} = B(T,z) \frac{\partial T}{\partial z} + C(T,z) \frac{\partial^2 T}{\partial z^2} + D(T,z) \qquad (19)$$

The backward difference method was used to approximate the time derivative and central difference for spatial derivatives. The equations were linearized by evaluating the coefficients B, C, and D at an intermediate time step. When

$$T_i^k = T(k\Delta t, i\Delta x)$$

Eq. (1() is approximated by

$$\frac{T_i^{k+1} - T_i^k}{\Delta t} = B_i^{k+1/2}\left[\frac{T_{i+1}^{k+1} - T_{i-1}^{k+1}}{2(\Delta z)}\right]$$

$$+ C_i^{k+1/2}\left[\frac{T_{i+1}^{k+1} - 2T_i^{k+1} + T_{i-1}^{k+1}}{(\Delta z)^2}\right] + D_i^{k+1/2} \qquad (20)$$

The resulting set of simultaneous algebraic equations was solved by using a standard tridiagonal matrix inversion. At each time step, the properties at k + 1/2 were evaluated, using linear interpolation between k and k + 1 levels. Iteration was performed at every time step, until the solution converged.

Discussion of Results

The input variables used in a typical run for the tip ignition program are given in Table 1. The computation is terminated when the propellant surface temperature reaches the specified ignition temperature of 850°K. Since no experimental or theoretical results are available in the literature for turbulent transport properties under highly

transient flow conditions, the initial selection of k_{eff}/k was somewhat arbitrary. However, it was selected because of its close agreement with one set of experimental data. In all later computations, the same value of k_{eff}/k was used.

TABLE 1. Input Variables for the
Tip Ignition Computer Program.

M_w	=	26.10 g_f/g-mole
γ	=	1.21
ρ_{pr}	=	1.71 g/cm^3
k_{pr}	=	0.80 x 10^{-3} cal/s-cm-°K
α_{pr}	=	0.0018 cm^2/s
T_f	=	3000°K
T_{ign}	=	850°K
T_i	=	298°K
T_{pi}	=	298°K
k	=	2.085 x 10^{-4} cal/s-cm-°K
k_{eff}/k	=	300
P_i	=	1033.23 g_f/cm^2

Figure 2 shows the ignition delay as a function of the pressurization rate at the crack tip. This figure also shows the comparison of predicted and measured ignition delays. The experimental setup and data reduction procedure are discussed in the section on Experimental Work. It can be seen that the ignition delay time decreases as the pressurization rate is increased. The slope of the curve is larger at the lower pressurization rates. The nature of the curve may help to explain why, at higher pressurization rates, the tip region of a real propellant crack may ignite prior to the arrival of the convective ignition front. At lower pressurization rates, the ignition delay time by this mechniism is much longer (>1 ms); therefore, the convective ignition front will reach the tip before the tip region ignites, due to stagnation point heat transfer associated with the compression waves and turbulent energy transport in the gas phase. However, as the pressurization rate is increased, the ignition delay time drops sharply, and under certain operating conditions, the ignition delay time may be smaller than the time for the ignition front to propagate to the tip. It should be noted that the numerical values of the ignition delay times and pressurization rates reported here should not be arbitrarily used for any crack geometry.

17
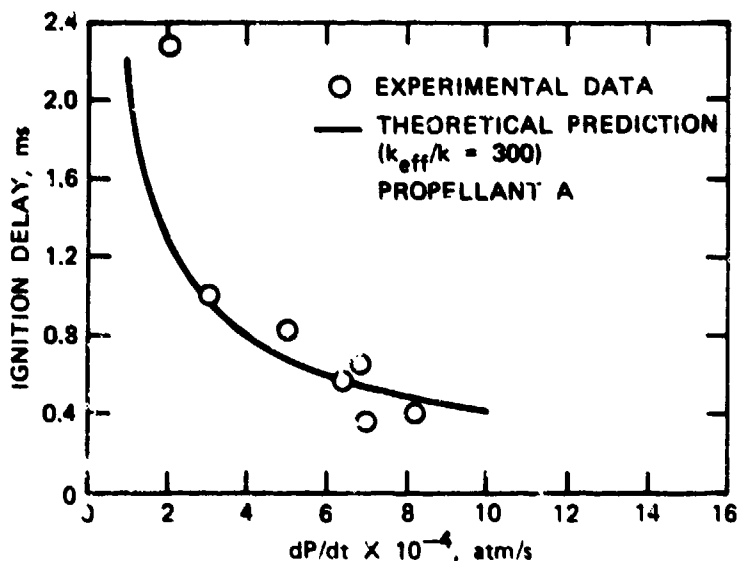
FIGURE 2. Comparison of Predicted and
Measured Ignition Delays.

The results for the tip ignition tests are for a given geometry and,
more importantly for an inert crack; the numerical values of the result
should, therefore, be used with caution. The theoretical predictions
are also dependent upon the value of k_{eff}/k. An increase in this ratio
will cause the ignition delay time versus pressurization rate curve to
shift downward, whereas a smaller value of k_{eff}/k will cause it to shift
upward. The validity of the theoretical model and the proposed physical
mechanism is supported by the good agreement between theoretical and
experimental results

Figure 3 presents a plot of propellant surface temperature and heat
flux to the propellant as a function of time for a given pressurization
rate. The propellant surface temperature increases almost linearly with
time, although it shows some curvature at the beginning. A higher pres-
surization rate would cause the slope of the curve to steepen, since,
for a higher pressurization rate, the ignition delay will be shorter.
The heat flux to the propellant surface also increases with time: as
time increases, the temperature gradient at the propellant-gas interface
steepens. The slope of heat flux versus time curve is higher in the
beginning and decreases with time. At a higher pressurization rate, the
curve will shift upward.
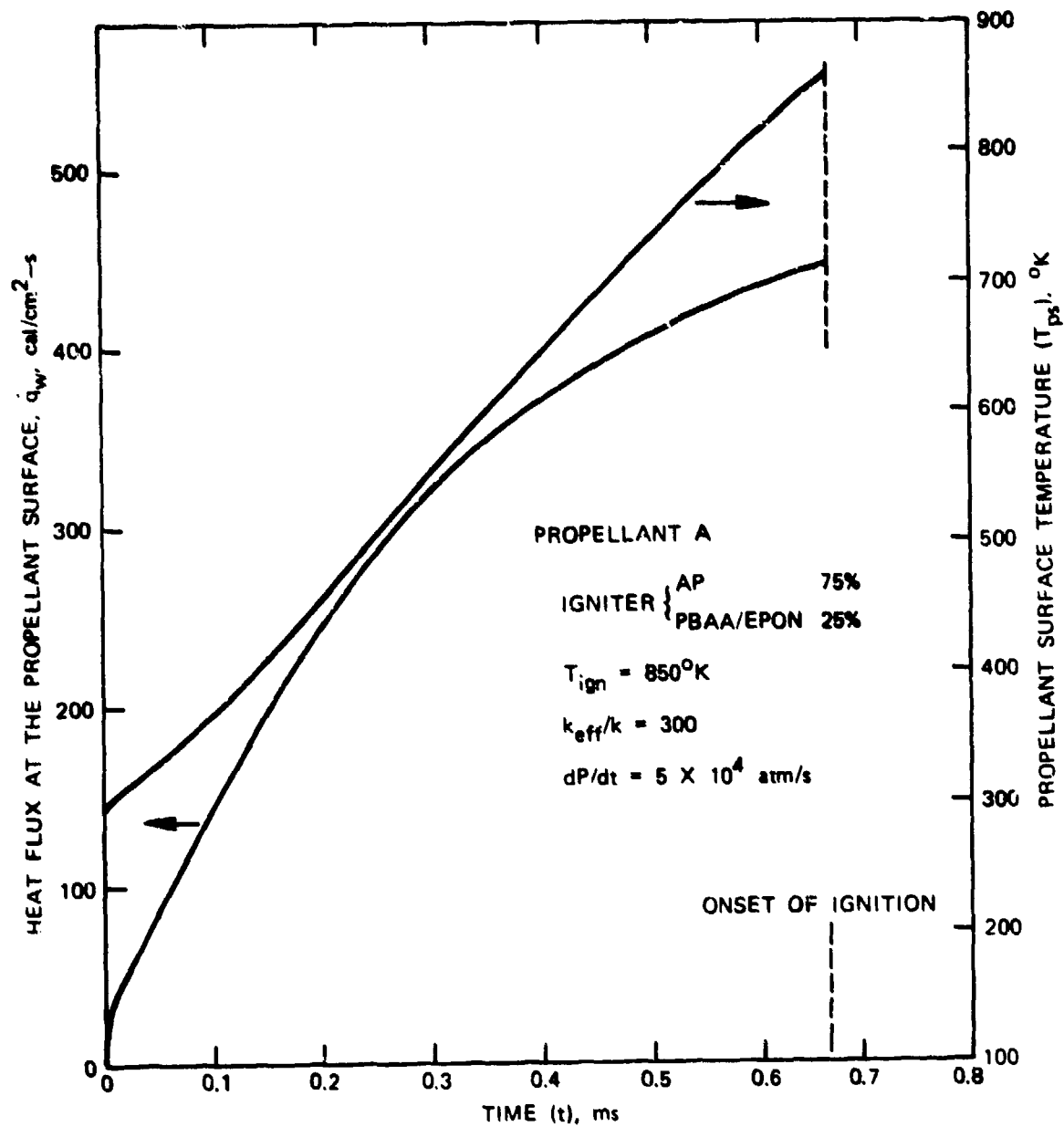
FIGURE 3. Calculated Heat Flux and
Propellant Surface Temperature vs.
Time.

19

The calculated temperature distribution at different times for a given pressurization rate is plotted in Figure 4. The temperature is plotted as a function of the transformed dimensionless coordinate, z, so that the detailed variations near the crack tip region can be illustrated. The temperature profile in the solid propellant shows that the gradient $(\partial T/\partial z)_{z=0}+$ [which is proportional to $(\partial T/\partial x)_{x=0}+$] steepens as time increases. The gradients near the interface appear to be steeper on the propellant side than on the fluid, because the effective (turbulent plus molecular) thermal transport coefficient for the gas is higher than that of the propellant. Although the high temperature region in the gas phase seems to be located at a considerable distance from the solid-gas interface, the actual physical distance to the high temperature region is only about 0.5 cm.

LINKAGE OF CRACK COMBUSTION CODE AND NONLINEAR FINITE ELEMENT ANALYSIS PROGRAM

Introduction

As mentioned earlier, for DDT in damaged propellant grains with cracks, crack branching/propagation is essential to provide the additional surface area for anomalous burning. A crack combustion program which can also predict stress concentrations at the tip is needed for realistic theoretical predictions of the accelerative burning inside the propellant crack, crack propagation, etc. Since the propellant is deformable, burning inside a solid propellant crack is basically a coupled solid mechanics and combustion phenomena. The combustion phenomenon inside the crack is strongly influenced by the crack geometry. The geometry, or gap width, can be altered for the following two reasons:

1. Mass loss due to gasification or ignition of the propellant surface along the crack during the combustion process, leading to a variation in the geometry.

2. Mechanical deformation of the propellant due to: (a) the pressure loading on the interior surface of the crack; (b) the pressure force of the combustion chamber acting on the propellant grain near the crack entrance; and (c) stresses in the propellant, due to pressure and temperature gradients in the grain, can also cause the crack geometry to change significantly.

Both the burning rate and the mechanical deformation are governed by pressure acting on the crack surfaces. On the other hand, a change in gapwidth or geometry will cause the pressure distribution to vary. This pressure distribution along the crack will strongly influence the deformations and stress concentration at the crack tip. It is obvious, therefore, that pressure and crack geometry are strongly interdependent in a burning solid propellant crack.
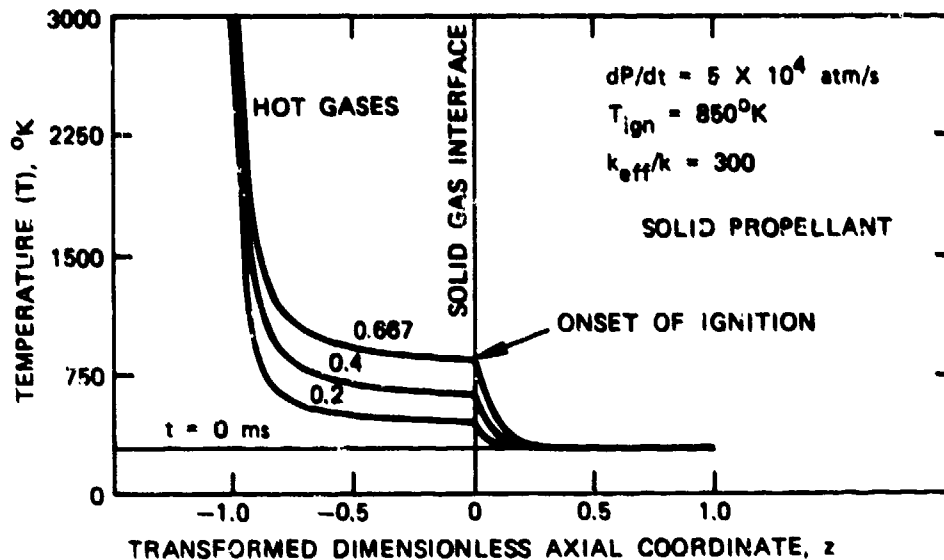
FIGURE 4. Calculated Temperature Distribution at Various Times.

In order to predict the effect of mechanical deformation on the ignition phenomena inside the crack, and at the same time the prediction of stress concentration at the crack tip due to a realistic pressure distribution along the crack, the crack combustion program was merged with a well-established structural analysis program. Of the numerous finite-element structural analysis program, the Nonlinear Finite-Element Analysis Program (NFAP) (a modified version of the NONSAP)[12,13] was considered most suitable for this study. This program is a user-oriented program which can be easily modified according to need. It is also capable of handling geometrical nonlinearities caused by the large deformations which are typical of propellants under high pressure. Another important feature of the program is its restart capability. The NFAP was modified to suit the needs of the current problem. A linear viscoelastic material model was added to the program in order to treat the mechanical properties of the propellants more realistically.

---

[12]University of Akron. *NFAP--A Nonlinear Finite Element Analysis Program*, by S. Prachuktam and T. Y. Chang. Department of Civil Engineering, Akron, Ohio, October 1976. (Report No. SE 76-3, publication UNCLASSIFIED.)

[13]K. J. Bathe and E. L. Wilson. "NONSAP--A Nonlinear Structural Analysis Program," *Nuclear Engineering and Design*, Vol. 29, No. 2 (1974), pp. 266-293.

Consolidation NFAP

For computational storage efficiency of the combined program, the original version of NFAP was modified and consolidated. The unnecessary portions of NFAP were deleted. In the input phase of NFAP, the subroutine for bandwidth reduction was deleted. Bandwidth reduction is essential for a structure whose geometry is very intricate and for which it is not manually possible to number the nodes in order to obtain the narrowest bandwidth. For our well-defined crack geometry, it was felt that the bandwidth reduction subroutine was unnecessary The subroutine for calculating three-dimensional pressure loading was also deleted. Since the propellant geometry being considered is two-dimensional, the subroutines for handling one-dimensional and three-dimensional input element data have also been deleted.

In the assembly phase of NFAP, the subroutines for the assembly of one-dimensional and three-dimensional stiffness matrices have also been removed. The original NFAP had several two-dimensional material models which were considered unnecessary, and, hence, were deleted. Instead, a two-dimensional linear viscoelastic material model was added. This will be discussed in detail in the next section. In the incremental solution phase of NFAP, once again the one-dimensional and three-dimensional equilibrium iteration subroutines have been deleted. The one-dimensional and three-dimensional stress calculation subroutines have also been eliminated. Deletion of these subroutines has resulted in a significant reduction in the size of NFAP, which, in turn, results both in a reduction in the storage space and in computational time and cost.

Viscoelastic Material Model

A linear viscoelastic material model has been implemented to describe the behavior of the propellant. The material behavior of the solid propellant is assumed to be viscoelastic in shear, and elastic in bulk. At present, only the isothermal condition is considered, and the viscoelastic response is assumed to be thermorheologically simple. The stress and strain tensors are defined as follows:

S_{ij} = stress deviators
e_{ij} = strain deviators
σ_{ij} = stress components
ε_{ij} = strain components

where

$$S_{ij} = \sigma_{ij} - 1/3\ \delta_{ij}\ \sigma_{kk} \tag{21}$$

$$e_{ij} = \varepsilon_{ij} - 1/3\ \delta_{ij}\ \varepsilon_{kk} \tag{22}$$

Then, the stress-strain relations with zero initial conditions are written in two parts.

The shear behavior is governed by

$$S_{ij} = \int_0^t G_1(\xi - \xi') \frac{d}{dt'} e_{ij}(t') \, dt' \tag{23}$$

where G_1 is the relaxation modulus in shear, and ξ is a "reduced time" due to the temperature above a reference state. For a constant temperature field, ξ is defined by

$$\xi = \phi(T)t \tag{24}$$

where ϕ is a shift function due to temperature effect on the viscoelastic behavior of the propellant. For most viscoelastic materials, it is usual to consider

$$G_1 = g_o + \sum_{m=1}^M g_m e^{-\beta_m t} \tag{25}$$

The bulk behavior is governed by

$$\sigma_{kk} = 3K \, \varepsilon_{kk} \tag{26}$$

where K is the bulk modulus.

For time-dependent structural analysis, it is necessary to form an incremental stress-strain relationship. When $(\ )^{t+\Delta t}$ is a quantity at time $t+\Delta t$ and $(\ )^t$ at time t, the incremental stresses, $\Delta\sigma_{ij}$, and strains, $\Delta\varepsilon_{ij}$, are defined by

$$\Delta\sigma_{ij} = \sigma_{ij}^{t+\Delta t} - \sigma_{ij}^t$$

$$\Delta\varepsilon_{ij} = \varepsilon_{ij}^{t+\Delta t} - \varepsilon_{ij}^t \tag{27}$$

Then, from Eq. (21) to (27), we can derive the incremental stress-strain relations in matrix form.

$$\{\Delta\sigma\} = [D_{VE}]\{\Delta\varepsilon\} - \{\sigma_o\} \tag{28}$$

where

$$\{\Delta\sigma\} = \{\Delta\sigma_{22}, \ \Delta\sigma_{33}, \ \Delta\tau_{23}, \ \Delta\sigma_{11}\}$$

$$\{\Delta\varepsilon\} = \{\Delta\varepsilon_{22}, \ \Delta\varepsilon_{33}, \ \Delta\gamma_{23}, \ \Delta\varepsilon_{11}\}$$

$$\{\sigma_o\} = \sum_{m=1}^M B_m \{_m C_{22}^t, \ _m C_{33}^t, \ _m C_{23}^t, \ _m C_{11}^t\} \tag{29}$$

23

and

$$[D_{VE}] = [D_{VE}]^T \begin{bmatrix} (K+2/3 \ A) & (K-1/3A) & 0 & (K-1/3 \ A) \\ & (K+2/3A) & 0 & (K-1/3 \ A) \\ & & A & 0 \\ & & & (K+2/3 \ A) \\ \text{Symmetric} & & & \end{bmatrix} \quad (30)$$

where

$$A = g_o + \sum_{m=1}^{M} g_m (1 - e^{-\beta_m \phi \Delta t})/(\beta_m \phi \Delta t) \quad (31)$$

$$B_m = 1 - e^{-\beta_m \phi \Delta t} \quad (32)$$

and the term $_m C_{ij}^t$ has a recursive relationship, i.e.,

$$_m C_{ij}^t = e^{-\beta_m \phi \Delta t} \ _m C_{ij}^{t-\Delta t} + \frac{g_m (1 - e^{-\beta_m \phi \Delta t})}{\beta_m \phi \Delta t} e_{ij}' \quad (33)$$

$$e_{ij}' = e_{ij}^t - e_{ij}^{t-\Delta t} \quad (34)$$

From the virtual work principle and the relationship of Eq. (28), one can derive the finite-element stiffness equations for a time interval [t, t+Δt],

$$[k]\{\Delta v\} = \{\Delta f\} - \{f_o\} \quad (35)$$

where Δv represents the increment of nodal displacement vector, and Δf the increment of applied nodal force vector. The element stiffness matrix is given by

$$k = \int [B]^T [D_{VE}] [B] \ dv \quad (36)$$

and f_o, a force vector due to the viscoelastic reponse of the material

$$f_o = \int [B^T] \{\sigma_o\} \ dv \quad (37)$$

where B is a strain-nodal displacement transformation matrix.

The material model described above has been written in the form of computer subroutines and these subroutines were implemented into NFAP for the purpose of conducting the viscoelastic analysis of solid propellant. A total of three new subroutines were prepared:

ELT2D9: Allocate array storages for calculating stresses, strains, and material matrix.

IVEL29: Initialize the arrays relating to the formation of the material matrix.

VSEL29: Calculate incremental stresses and strains and form the viscoelastic material matrix.

For the validation of the viscoelastic material model, the program was tested for some simple cases for which analytical solutions were available. The agreement between the numerical and analytical solutions was excellent.

For actual computations of the combined program, the material properties were obtained from Mr. C. F. Price of NWC, China Lake, California. They are as follows:

$$K = 700,000 \text{ psi}$$

$$G_1 = 212 + 654 \exp(-0.095t) \text{ psi} \tag{38}$$

Combination of NFAP and CCC

Approach. For the transient burning inside a solid propellant crack, many interrelated physical phenomena should be considered in the theoretical modeling. The combination of convective burning and structural mechanics analyses can be very complex. Some of the interdependent processes are:

1. Pressure inside the crack results in a deformation of the propellant crack geometry.

2. During combustion, there is mass loss due to the gasification of the propellant surface inside the crack, and this changes the geometry of the crack.

3. Deformation of the propellant crack geometry causes the pressure to change.

4. Pressure wave phenomena is interdependent with the transient variation in the crack geometry.

5. Compression of the propellant may alter its burning characteristics.

6. The temperature gradients involved in the convective burning may cause thermal stresses in the solid, contributing to crack propagation.

7.   The structural analysis should account for the mass loss and the effect of surface ablation on the stresses in the solid.

It is obvious that the coupling between the pressure along the crack and the deformation is the most important, and that it could influence the combustion phenomena significantly. Some of the other coupled processes mentioned above are of secondary importance and are ignited in the present analysis. The thermal stresses due to the temperature gradients are considered to be small when compared with the mechanical stresses caused by deformation alone. Variation in the burning rate due to compression of the propellant may not be significant, considering the strong dependence of the burning rate on pressure.

Incorporation of the mass loss of the propellant into the structural analysis may be important, but it is quite involved, requiring extensive program revisions. However, it should be noted that for the region of interest of our analysis, i.e., during the early phase of combustion before substantial burning takes place, ignoring mass loss in the structural analysis may be justified. During this period, the geometry variation due to surface gasification is small when compared to the variation due to mechanical deformation, which, of course, is accounted for in the program.

In the present solution scheme, the pressure and the deformation are not solved simultaneously. They are obtained independently at a finite time interval apart, i.e., pressure at time t_1 is used as an input to determine the deformation at time $t_1 + \Delta t$. In other words, a time lag is introduced between the pressure computations obtained from CCC, and the deformation computations obtained from NFAP. The smaller the time lag, the more accurate the solution will be. A schematic diagram of the coupling is shown in Figure 5. It is believed that the time lag between the pressure and deformation computations will result in only negligible errors. In fact, it may even be justified on the grounds that the material would require some finite time lag to respond to an applied pressure load. Also, these time lags are usually smaller than a few hundreds of the total event time, and, therefore, may not have a very significant effect on the overall solution.

Implementation of the Combined Program. The initial implementation of the combined program included such considerations as input and output data, an overlay structure to conserve memory core, and organization of COMMON storage areas to transfer necessary data between the two programs. A system of interfacing-subroutines were used to transfer program control between the NFAP routines and the CCC routines. When coupling the two programs, the approach was to keep them as separate as possible, for the following two reasons. First, if modifications to CCC are made, program modification and testing can be made for CCC alone, and NFAP and CCC can be recoupled without further revisions. This

26

CCC — PRESSURE DEPENDS ON TIME HISTORY AND
DEFORMATION OF GAP WIDTH

NFAP — MECHANICAL DEFORMATION IS A FUNCTION
OF PRESSURE AND TIME

CCC/NFAP — COUPLED COMBUSTION AND SOLID
COMBINATION MECHANICS SOLUTION FOR ANY SPECIFIED
INCREMENTAL TIME STEP
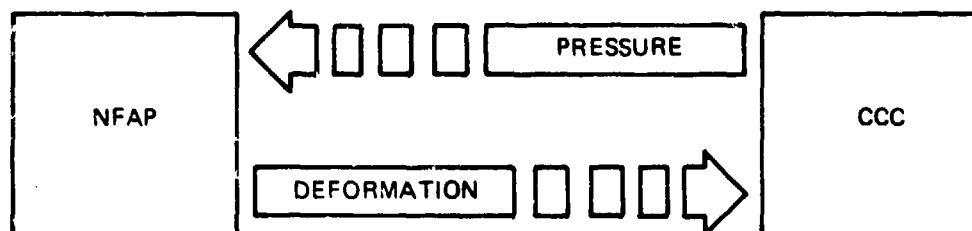
FIGURE 5. Schematic Diagram of CCC and NFAP Linkage.

improves the efficiency of any program testing, and allows the greatest
flexibility in program verification. Similarly, NFAP can be tested
alone, with a coupling to CCC, or with an artificial pressure loading
routine, in order to perform solid mechanics studies. A second reason
for maintaining the two programs separately is to keep NFAP and CCC as
close to their original forms as possible. In this way, others can
utilize the programming procedures developed, substituting their own
procedure for convective burning or structural analysis, if desired,
without formulating a new linkage. These considerations increase the
potential usefulness of the combined program by keeping it general and
versatile.

The disadvantages of this approach are minimal. The greatest
disadvantage of keeping NFAP and CCC as complete as possible is the need
for increased program memory size. Both are large programs, with large
core storage requirements. This limitation, however, can be relaxed by
utilizing a memory overlay structure to conserve memory core for program
use. Since the two halves of the combined NFAP/CCC program are executed
alternately, only one half needs to be in memory at any given instant
during the execution of the program. That is, while the structural
analysis is taking place during the execution of the combined program,

the convective burning routine is not immediately needed, so the space
in memory is overlaid by the NFAP routines. Similarly, when the con-
vective burning analysis is taking place, the NFAP routines not in
execution at that time are replaced in core by the CCC routines. The
penalty of increased execution time due to the transfers between memory
core and an intermediate input/output device (direct access magnetic
disk) is small when compared to overall execution time. The overlay
procedure is automatic and independent of the program. The operating
system for the IBM Model 370 computer used for all the computations
includes an overlay feature which requires only an outline of the over-
lay structure and some control cards. The use of the overlay feature
was not critical for any of the analyses performed on the IBM 370 com-
puter at Pennsylvania State University because of the large memory
capacity (1000 k bytes of storage to a single program) available. The
core size specification of the operating system allowed maximum avail-
able storage and, consequently, the overlay feature was not needed for
the computations. At other computer installations, however, core size
limitations are usually very critical, and an overlay structure will be
necessary.

The theoretical coupling considered between the convective burning
and structural analysis is simplified, as previously discussed, to the
transfer of pressure loading and crack deformation. Pressure is calcu-
lated by the CCC portion of the combined program at each nodal point
location on a one-dimensional grid along the length of the crack. The
convective burning analysis of the crack combustion incorporates the
crack geometry variation caused by both mechanical deformation and mass
loss through gasification of the propellant surface. Once the gas
phase equations are solved and pressures along the crack are calculated
for a particular time t, program control is transferred to the NFAP
portion of the combined program. The surface elements in the finite
element mesh are then loaded with the pressure calculated in CCC. NFAP
updates the stiffness matrix, performs a static analysis at time t, and
calculates the propellant deformation. The change in the crack width at
each finite-difference node is calculated and added to the existing
crack width. Control is transferred back to CCC, the next time itera-
tion $(t + \Delta t)$ is made, and control is again transferred to NFAP. In
this manner, pressure and changes in crack width are coupled. The
general layout of the linkage is shown in Figure 6.

Some modifications to the procedure described above are necessary
due to considerations of execution time efficiency. The time required
for NFAP to complete a static analysis is approximatly an order of
magnitude higher than the execution time for one CCC time iteration.
Although CCC uses an implicit solution method, the time must be small
enough to give accurate results. Performing structure analysis for
every iteration in CCC is prohibitive in view of the extremely long
computer time required. An option of the combined program coupling is
to specify the number of time iterations CCC will complete before
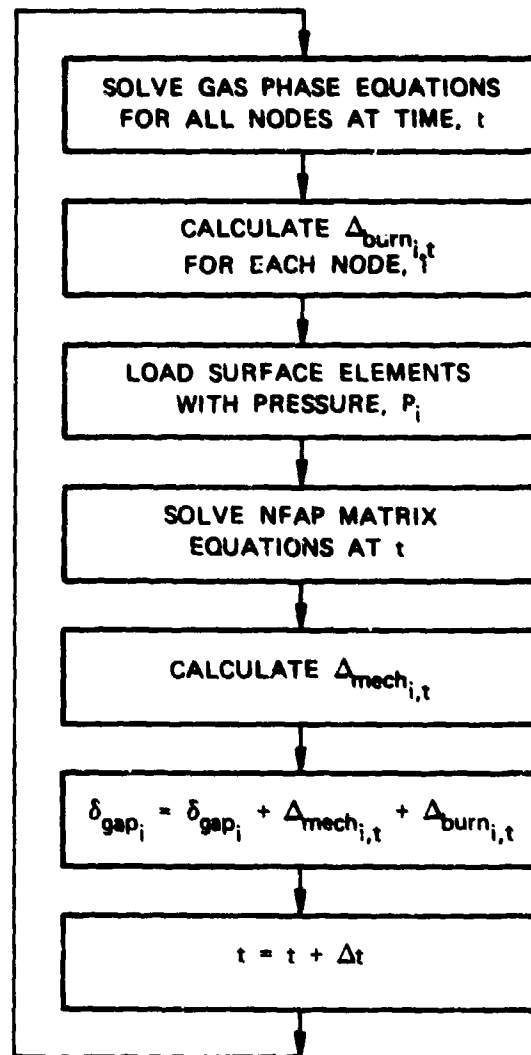
FIGURE 6.   General Layout of the CCC and LFAP Linkage.

transfer is made to NFAP for an updating of the crack width. When
CCC takes more than one time step between crack-width updating, the
change in crack width is averaged over the time increments before addi-
tion to the existing width. For example, if CCC completes ten itera-
tions before transferring control to NFAP for an updating of crack
geometry, one-tenth of the change in deformation returned by NFAP will
be added during the next ten iterations in CCC. This averaging approx-
imation is designed to smooth out any step changes in the geometry that
would affect the CCC solution convergence. The allowable number of
iterations in CCC between transfers to NFAP is, in general, dependent on
the time increment, chamber pressurization rate, and crack width.

The general stress-strain equations are solved using a plane-strain
analysis. This is compatible with the experimental test configuration,
in which the propellant is confined from all sides except the entrance.
The transient nature of the pressure loading is considered by using a
static analysis at incremental time steps. A static analysis was chosen
because of the prohibitive computational times involved and the complex
nature of dynamic analysis. However, the options of using the dynamic
analysis is available.

Formulation of the Finite Element Mesh. The analysis considers a
two-dimensional configuration, which is compatible with the crack geom-
etry considered in the convective burning model in the crack combustion
code. Two-dimensional continuum elements were used to model a sample
crack. Because of symmetry about the crack centerline, only one half
of the solid-propellant crack model needs to be considered. Figure 7 is
a diagram of a finite element grid for a sample problem. The element
mesh near the crack entrance was slightly modified. The square corner
at the entrance of the crack was rounded a bit, and the grid was refined
somewhat for better computational accuracy. Each isoparametric, quad-
rilateral element contains eight nodes, four nodes at the corners and
one node at the midpoint of each side. This feature of NFAP makes it
possible to reduce the number of elements needed to produce accurate
results. Equal accuracy may thus be achieved with less computational
effort than is necessary with four-node elements. During the initial
testing of the program, a simplified element grid was used, with only
one layer of elements instead of the present configuration of four layers
in the axial direction of the crack. Multiple layers are used in order
to increase the accuracy of the solution.

The finite-difference nodes used in the CCC one-dimensional grid
are in a one-to-one correspondence with the finite-element nodes which
form the propellant surface in the NFAP two-dimensional mesh. This
allows one to transfer the deformations obtained from NFAP directly to
CCC. The model grid is stressed by applying pressure loading to the
appropriate surfaces, and fixing boundary conditions to the elements.
The transient pressure loading for the individual elements along the
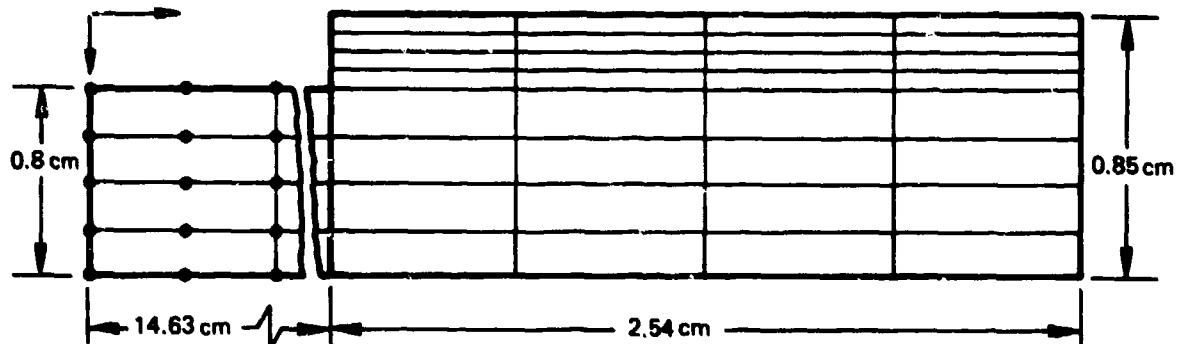
FIGURE 7. Finite Element Grid.

crack surface is determined by the crack combustion routine. The load-
ing at the entrance of the crack is determined by the chamber pressure,
given as a function of time. The schematic diagram of the pressure
loading and boundary conditions of the model grid is shown in Figure 8.
All surfaces of the propellant mesh are either pressure loaded or have
fixed boundaries. The propellant at the tip of the crack is fixed in
one direction only, due to the symmetry of the mesh. Along the surfaces
of the propellant in contact with the brass mold, the boundaries are
assumed fixed.

Pressure data from the convective burning analysis are available at
the finite-difference nodes. Pressure input to NFAP, however, must be
in the form of uniform pressure loading on individual element surfaces.
Every element surface is defined by three nodes: two nodes at the
endpoints of the elements, and one node at the midpoint of the surface.
The uniform surface loading of an element is obtained from the spatially-
weighted average of the pressures at the three surface nodes. Although
there is a one-to-one correspondence between the finite-element and
finite-difference nodes along the surface of the crack, the pressure
profile considered by NFAP contains discontinuities at each element
boundary along the surface, because of the pressure averaging procedure.

Pressure loading of the two-dimensional elements at the entrance
and the tip of the crack also involved side loading, i.e., loading in
the axial direction of the crack. The side loading of the surface
elements at the opening of the crack was determined by the chamber
pressure at any given time. Side loading at the tip of the crack was
considered the same as pressure loading on the last element along the

surface of the crack. Appendix C lists the input format and Appendix D the sample data for the combined program.
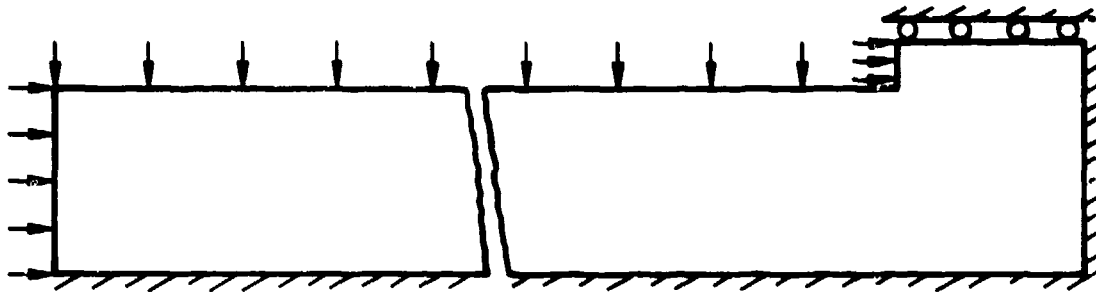
FIGURE 8. Boundary Condition for a Test Specimen.

Discussion of Results. Some preliminary computations were made with the combined structural analysis and convective burning program. The results obtained from the combined program were compared with those obtained from convective burning analysis alone. From these comparisons, it was possible to draw some general conclusions. A more detailed analysis of the results from the combined program is being performed under the second phase of the contract.

The crack geometry used for the combined NFAP/CCC program is compatible with the dimensions of the propellant test specimen used for experimental test firings. The primary inputs to the program are the chamber pressurization rate and the crack geometry. For preliminary test runs, the initial geometry of the crack has a uniform rectangular-cross-sectional area. The chamber pressurization rates are assumed to be constant, i.e., the chamber pressure is a ramp function of time. For a very low chamber pressurization rate, the effect of the mechanical deformation is relatively insignificant on the combustion process inside the crack.

The chamber pressurization rate is 5×10^5 atm/s for the result reported here. It should be pointed out that the constant pressurization rate used is quite close to that observed experimentally, especially over the period of interest. In an actual test firing, the chamber pressure rises at a nearly constant rate, remains steady for a long period of time, and then falls. The calculation is continued until the pressure reaches the peak chamber pressure.

Calculated pressure distributions at various times, from the convective burning analysis alone, are shown in Figure 9. As time progresses, the chamber pressure increases, hot gases enter the crack, and pressure waves travel along the length of the crack. As the hot gases flow over the propellant surface, the surface temperature increases until surface ignition occurs. Propellant mass loss through gasification causes increased pressure, which enhances the burning rate. The combustion gases, driven by the pressure gradient, penetrate deeper into the crack, causing the ignition front to propagate. The locus of the ignition is shown by the dashed line on the same figure. At 232.5 μs the ignition front has propagated through 60% of the crack length.
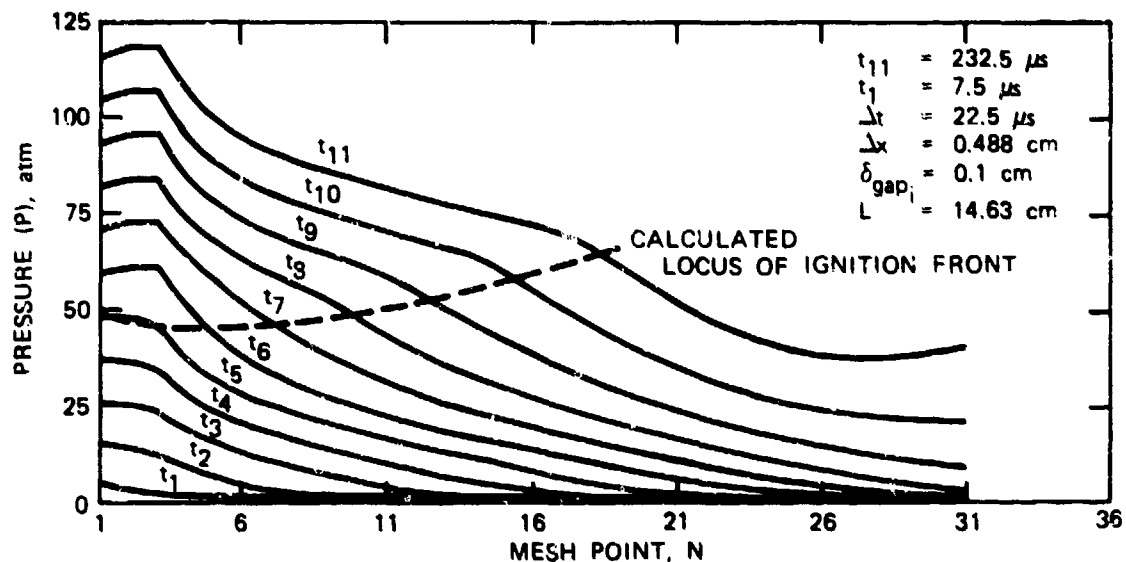
FIGURE 9. Calculated Pressure Distributions
for Various Times From the Crack Combustion
Code.

Using the same initial geometry and pressurization rate, the test case was run again, but with the coupled convective burning and structural analysis program incorporating the linear viscoelastic model. The pressure distributions and the locus of the ignition front calculated from the combined NFAP/CCC program is shown in Figure 10. The general trends of pressure with respect to time are similar to those from the convective burning analysis alone, but when the pressure inside the crack increases above 25 atm, the pressure distributions from the two analyses begin to differ. The pressure obtained from the combined analysis generally increases faster than the pressure calculated by the

33
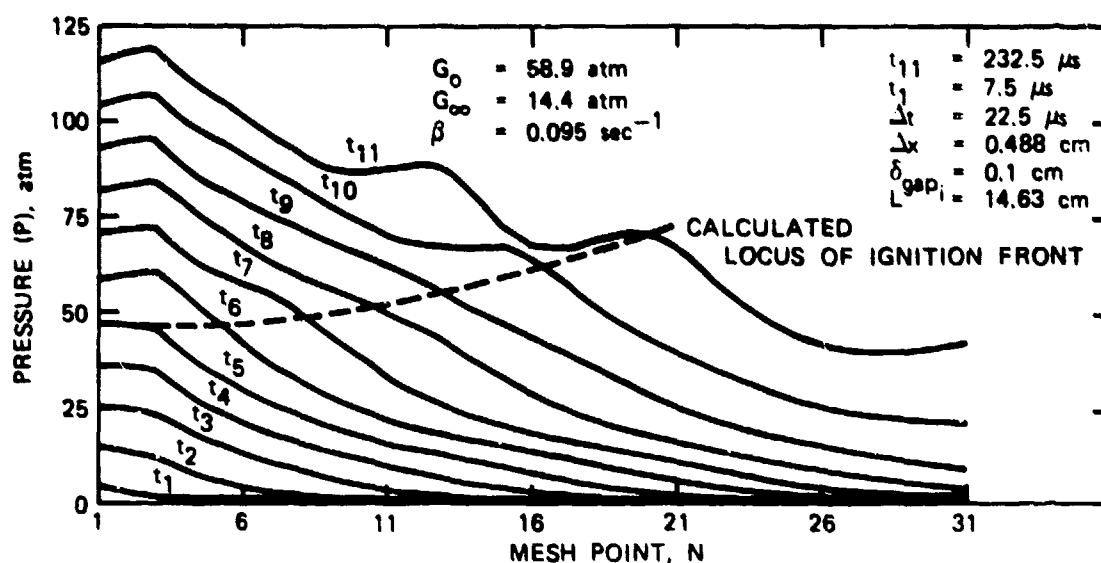
FIGURE 10. Calculated Pressure Distributions for Various Times From the Combined Crack Combustion and Nonlinear Finite-Element Analysis Program.

convective burning program alone. This can be explained by an examination of the port area variation along the crack. The increased pressure corresponds to a reduction in the area of the flow channel. The physical explanation of the decrease in crack width in the combined analysis is based on the solid mechanics consideration. Because of the pressure loading on the elements at the entrance of the crack and the constraints along the boundaries, the deformation of the propellant was fairly complicated. The elements at the entrance, compressed by the chamber pressure, deform inward, pushing the propellant into the crack. Since the chamber pressure increases faster than the pressure inside the crack during the early stage, the propellant is pushed towards the lower pressure region inside the crack. The mechanical deformation of the propellant causes the narrowing of the crack width.

As time progresses, the pressure distribution becomes wavy in shape, causing the propellant surface also to become wavy. The localized pressure rises correspond to the deformation of the propellant along the crack. The pressure and port area display a very strong inverse relation. Propagation of the localized pressure phenomena along the crack toward the tip can be seen in Figure 10. At 232.5 μs, the

localized pressure phenomena, evident around nodes 12 and 20, are increasing in magnitude. The locus of ignition front exhibits a slightly faster rate of propagation into the crack, as compared to that shown in Figure 9. It is interesting to note that the result obtained from the coupled program does not necessarily give lower pressure inside the crack or a lower flame propagation rate.

DETERMINATION OF COMPLETE SET OF DIMENSIONLESS PARAMETERS

The nondimensionalized governing equations for the gas-dynamic and heat-transfer equations were reported in the last annual report,[2] and will not be repeated here. The nondimensional equations for the solid mechanics portion, and the resulting dimensionless parameters will be given here. The equation for stresses in the solid under equilibrium conditions is:

$$\frac{\partial \sigma_{ij}}{\partial x_j} = 0 \tag{39}$$

the constitutive law for linear viscoelastic materials is:

$$\sigma_{ij}(t) = \int_{-\infty}^{t} G_1(t - \tau) \frac{d}{d\tau} \epsilon_{ij}(\tau) d\tau$$

$$- 1/3 \, \delta_{ij} \int_{-\infty}^{t} G_1(t - \tau) \frac{d\epsilon_{kk}}{d\tau} \, d\tau + 1/3 \, \delta_{ij} K \epsilon_{kk} \tag{40}$$

where the relaxation modulus in shear, G_1, can be expressed as

$$G_1(t) = G_\infty + (G_o - G_\infty) e^{-\beta t} \tag{41}$$

Defining the dimensionless parameters as follows

$$\tilde{t} \equiv \frac{t}{t*} \tag{42}$$

$$\tilde{\sigma}_{ij} \equiv \frac{\sigma_{ij}}{\sigma*} \tag{43}$$

$$\tilde{x}_j \equiv \frac{x_j}{\lambda}$$

$$\tilde{G}_o \equiv \frac{G_o}{P*} \quad , \quad \tilde{G}_\infty \equiv \frac{G_\infty}{P*} \tag{44}$$

$$\tilde{K} \equiv \frac{K}{P\star} \tag{45}$$

The reference quantities selected are given below (see Ref. 1 for details)

$$t\star \equiv \frac{\lambda_{pr}^2}{\alpha_{pr}h_c\star^2} \left[\frac{T_{ign} - T_i}{T_f - T_i}\right]^2 \tag{46}$$

$$\sigma\star = \frac{K_{I_c}}{\sqrt{L}} \tag{47}$$

$$\ell = \ell_{web} \text{ for the transverse coordinate} \tag{48}$$

$$P\star = \left[\frac{a}{\Gamma(\gamma)}\left(\frac{A_{b_i}}{A_{p_i}}\right)\rho_{pr}\sqrt{\frac{RT_f}{g}}\right]^{1/(1-n)} \tag{49}$$

where

$$\Gamma(\gamma) \equiv \sqrt{\gamma \frac{2}{\gamma + 1}^{\frac{\gamma+1}{\gamma-1}}} \tag{50}$$

After nondimensionalization, the equilibrium equation for stresses in solid propellant becomes:

$$\frac{\partial \tilde{\sigma}_{ij}}{\partial x_j} = 0 \tag{51}$$

The constitutive law for linear viscoelastic material becomes

$$\tilde{\sigma}_{ij}(\tilde{t}) = \left(\frac{P\star \ L}{K_{I_c}}\right)\left\{\int_{-\infty}^t \tilde{G}_1(\tilde{t} - \tilde{\tau}) \frac{d}{d\tilde{\tau}} \tilde{\varepsilon}_{ij}(\tilde{\tau})d\tilde{\tau}\right.$$

$$- 1/3\delta_{ij}\int_{-\infty}^t \tilde{G}_1(\tilde{t} - \tilde{\tau})\frac{d\tilde{\varepsilon}_{kk}}{d\tilde{\tau}} d\tilde{\tau}$$

$$\left.+ 1/3\delta_{ij}\tilde{K}\ \varepsilon_{kk}\right\} \tag{52}$$

and

$$\tilde{G}_1(\tilde{t}) = \tilde{G}_\infty + (\tilde{G}_o - \tilde{G}_\infty)e^{-(\beta t\star)\tilde{t}} \tag{53}$$

36

Finally, the complete set of dimensionless parameters can be put into the following form

$$\frac{u_{fp}}{u^*} = \frac{u_{fp}}{u^*} \left\{ \frac{\alpha_{pr}}{r_b^{*2}P_c} \left(\frac{dPc}{dt}\right)_i \quad, \quad \frac{\delta_{fs}}{\delta_{gap}} \quad, \quad B_i^* \quad, \quad B_m^* \quad, \quad \frac{\rho_{bi}}{\rho_{wi}} \quad, \right.$$

$$\frac{L}{D_{H_i}} \quad, \quad M^* \quad, \quad St^* \quad, \quad \frac{T_{ign} - T_i}{T_f - T_i} \quad, \quad \frac{L}{\ell_{web}} \quad, \quad \frac{\epsilon}{D_{H_i}} \quad, \quad Re^*_{D_{H_i}} \quad,$$

$$\left. \frac{r_{c_{tip}}}{L} \quad, \quad \frac{G_o}{P^*} \quad, \quad \frac{G_\infty}{P^*} \quad, \quad \frac{K}{P^*} \quad, \quad \frac{K_{I_c}}{P^*\sqrt{L}} \quad, \quad \text{and} \quad \infty t^* \right\} \qquad (54)$$

EXPERIMENTAL WORK

CRACK TIP IGNITION STUDY

In the last annual report,[1] it was noted that a bright spot near the tip region of the propellant crack was observed before the convective ignition front reached the tip. The existence of this spot can be attributed to one of the following conditions.

1.   Ignition of combustible species evaporated from the propellant surface near the crack entrance region and transported to the propellant tip by the initial pressure gradient.

2.   Ignition or combustion of the unreacted species from the igniter system carried to the crack tip by the initial pressure gradient.

3.   Ignition of the propellant tip region by a mechanism other than items 1 or 2 mentioned above.

In order to experimentally investigate the phenomena of crack tip ignition, an inert crack was formed, as shown in Figure 11. It was designed to have inert surfaces along the crack, with a propellant sample only at the tip. Some modifications were made in the combustion chamber to accommodate the desired geometry. The crack was formed between a thick plexiglass window and the bottom surface of the crack combustion chamber. To examine any material loss of the propellant at the tip, some go/no-go tests were conducted for such a configuration. In all these tests the propellant sample burned and mass loss were observed. Since the tests were done for the inert crack, there was no possibility of any combustible species evaporating from the crack entrance

37
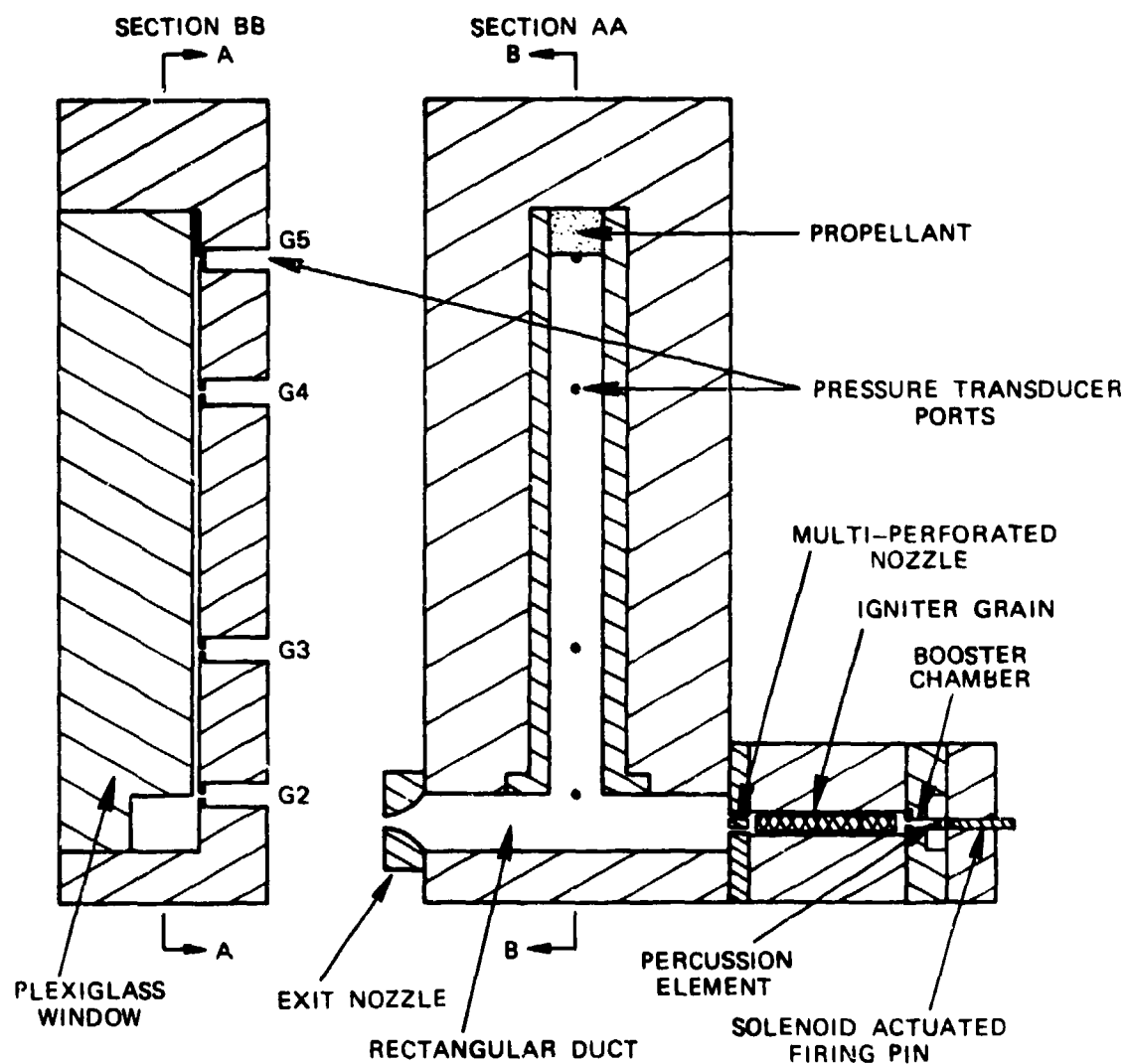
FIGURE 11. Schematic Diagram of the Test Rig
for the Study of Propellant Ignition at the
Closed End of an Inert Crack.

and then reacting at the tip. Therefore, it was possible to rule out
the first mechanism mentioned (item 1). The tests were also conducted
with inert material, e.g., silicon rubber or clay, instead of propellant
at the tip of the inert crack. High speed motion pictures of these
tests revealed no bright spot near the tip region, thereby eliminating
the possibility of the reaction of some of the combustible species from
the igniter system.

These observations confirm the fact that the previously observed
and reported bright spot in a propellant crack is not caused by further
reaction of fuel and oxidizer species resulting from the incomplete
combustion of the propellant near the entrance region of the crack or
from the igniter system. The bright spot represents the actual ignition
of the propellant at the crack tip. As explained in the section entitled
Theoretical Work, the mechanism of tip ignition appears to be caused by
the enhanced transport of energy in the gas phase which is driven by
strong compression waves.

Numerous experimental test firings were conducted to obtain the
effect of pressurization rates on the ignition delay time. Propellant A
was used as the test propellant in all tip-ignition tests. A schematic
diagram of the combustion chamber is shown in Figure 11. The rectangular
cross-sectional channel simulating the crack was placed normal to the
flow direction in the chamber. A pair of brass strips was placed be-
tween the bottom surface of the combustion chamber and the innermost
plexiglass window to form the crack. The gap width of the crack could
be varied by using brass strips of different thicknesses. For all
results reported here, the same pair of brass legs were used. The gap
width of the crack thus formed was 0.051 in. (1.3 mm). The length of
the crack was about 7.48 in. (190 mm) and the width was 0.37 in. (9.4
mm). Use of the plexiglass window as one of the surfaces of the channel
facilitated an unobstructed view of the ignition phenomena. The chamber
was completely sealed, except for the interchangeable exit nozzle through
which the product gases were discharged to the atmosphere. The chamber
was designed for a maximum static pressure of 800 atm. In this study,
however, the maximum pressure was only about 200 atm.

A solid propellant igniter system was used as a source for hot gas
generation. Percussion primers were used as the initiators for ignition
of a propellant strand. A solenoid-activated firing pin was used to
trigger the primer. When the primer is triggered, the hot gases flow
over the propellant strand and ignite it. The product gases flow through
a multi-perforated converging nozzle into the main chamber. The pressur-
ization rate of the chamber can be varied by altering the dimesions of
the propellant strip in the igniter, by changing the dimensions of the
multiperforated nozzle, or by changing the exit nozzle of the chamber.
In the present study, pressurization rates up to 8×10^4 atm/s were
obtained at the crack tip.

A block diagram of the remotely controlled ignition and high-speed
photography system is shown in Figure 12. The solenoid which triggers
the percussion primer is activated by an event-switch built into the
high-speed camera. After the camera is switched on, a few milliseconds
are required to reach the desired framing rate. This delay time can be
related to the footage of the film that passes through the camera before
the attainment of the prescribed framing rate. The event switch of the
camera is controlled by a footage indicator. During the operation, the
footage indicator is set to a preselected value corresponding to the
desired framing rate. After a certain length of film (preset on the
footage indicator) runs through the camera, the event switch closes,
thereby activating the relay. The relay, in turn, activates two other
switches; one triggers the solenoid to initiate the ignition event, and
the other closes the common-time switch on a light emitting diode (LED)
driver unit. At the instant when the common-time switch closes, the LED
driver unit generates a 2 ms pulse. The pulse is recorded on a magnetic
tape and is simultaneously marked on the film. These common-time marks
are used for the time correlation of the data recorded on the tape and
the film.

The data acquisition system consisted of two major parts: (1) the
pressure recording system, and (2) the ignition event recording system.
A block diagram of the data acquisition system is shown in Figure 13.
Pressure measurements were taken at four locations along the crack, in-
cluding one at the crack entrance and another at the tip. Piezoelectric
quartz transducers (Kistler model 601 B) were used to measure the pres-
sure. These transducers have a rise time of 1.5 µs, natural frequency
of 300 kHz, and can accurately record pressures up to 18,000 psi (1225
atm). The transducers were mounted in a water-cooled adapter (Kistler
model 628C) which prevented drifting or damage caused by excessive heat.
The signals from the pressure transducers were carried through an in-
sulated, high-impedance, coaxial cable [Model 121 M(x)] with a capaci-
tance of 30 pF/foot, to a charge amplifier (Kistler model 504E). The
amplified signals were recorded on FM channels of a 14-channel AM/FM
tape recorder (Hewlett-Packard model 3924B).

Two separate systems were used to simultaneously record the igni-
tion event. A high-speed, 16-mm, motion picture camera (Hycam Model
K20S4E-115) was used to observe the complete ignition event in the
chamber. The camera was capable of filming at a maximum of 16,000
pictures per second and was equipped with a dual LED timing system which
recorded the common-time and timing marks on the film. The LED driver
unit, a common-time pulse and high frequency (up to 10 kHz) timing
generator, was used to operate the LED timing system. A photodiode
system was also used to observe ignition at the tip. A camera lens
(Schneider-Kreuznauch, 150 mm) was used to focus the tip region onto a
photodiode (E.G. and G. model SGD040A). When the tip region is ignited
the photodiode gives out a signal which is amplified and recorded on the
magnetic tape.
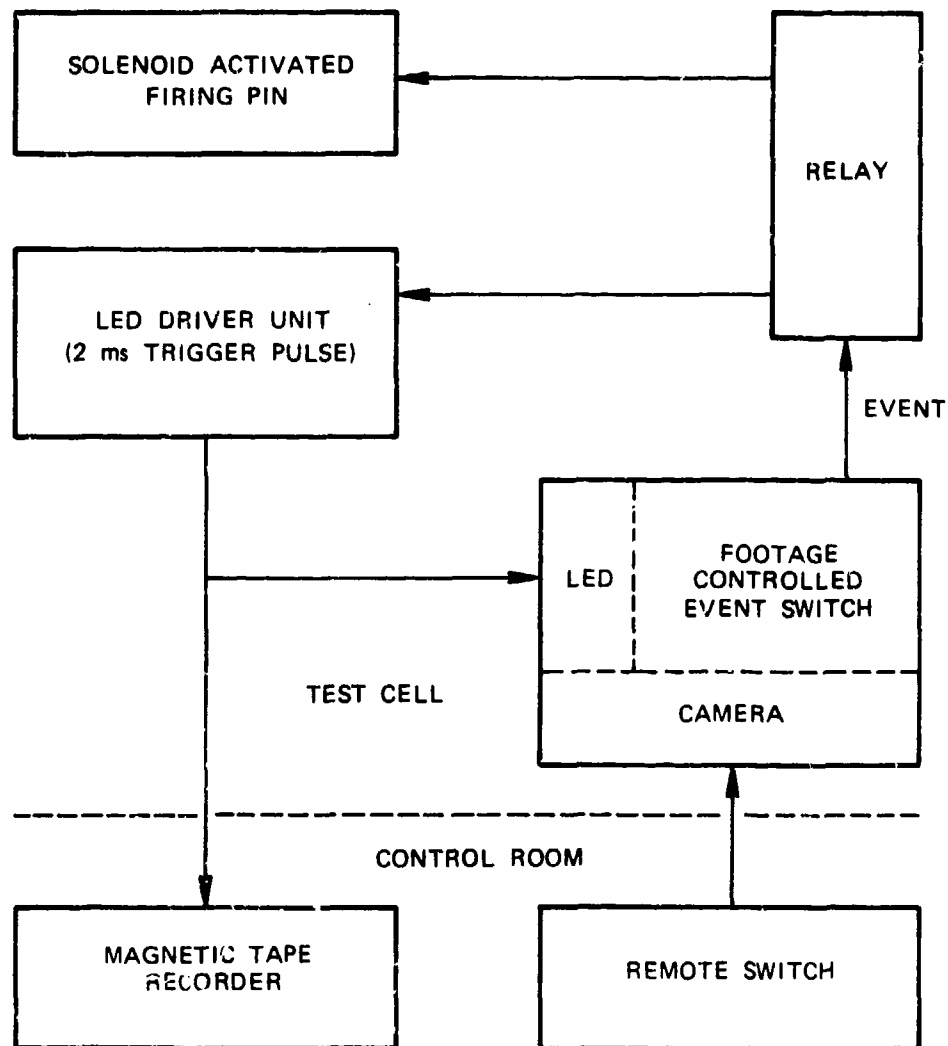
FIGURE 12. Block Diagram of Remotely-Controlled
Ignition and Photography System.
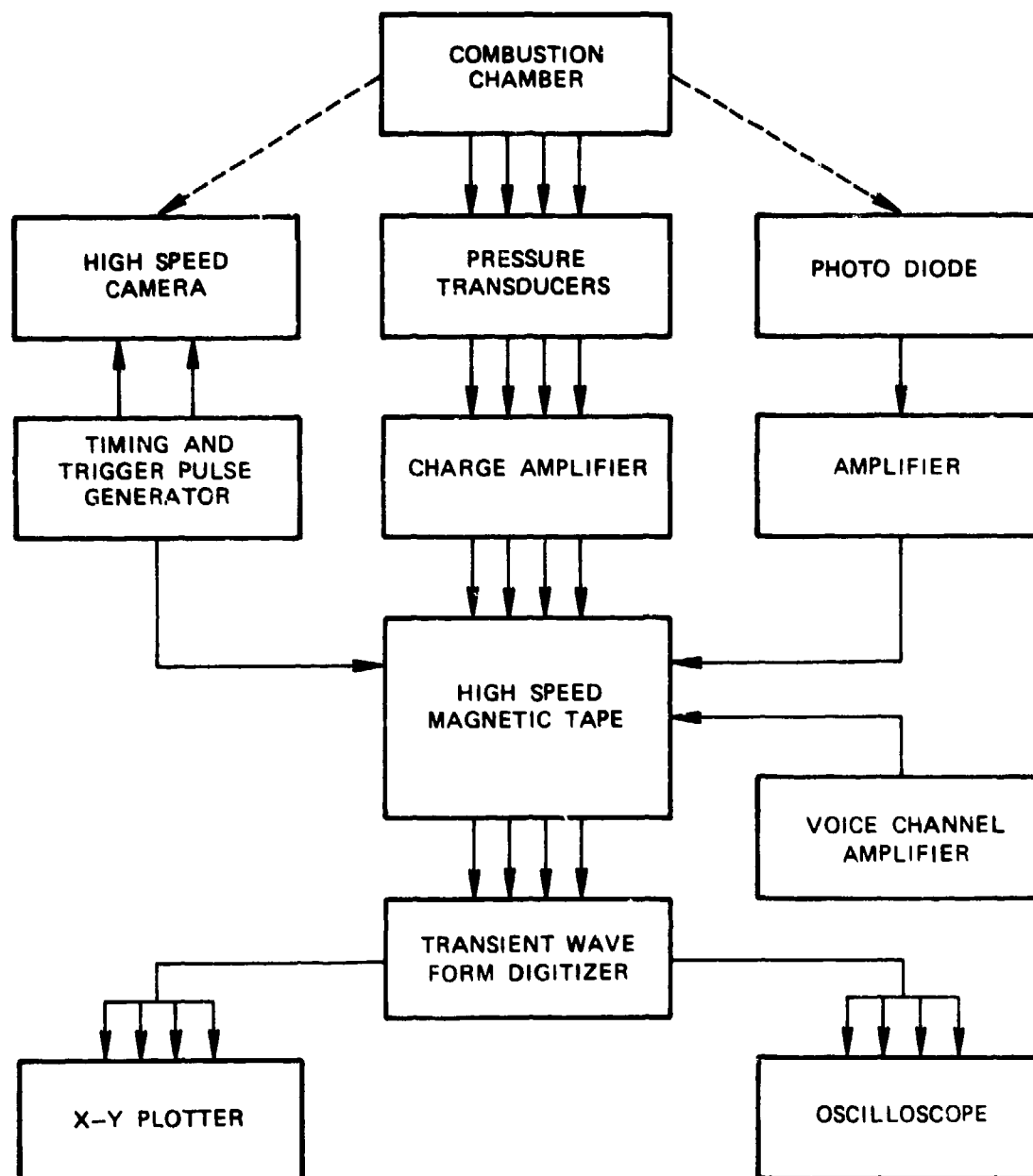
FIGURE 13.   Block Diagram of Data Acquisition System.

The data recorded on tape were digitized using a 4-channel Bioma-
tion Model 1015 waveform digitizer with a 1024-word memory per channel,
and a capability of maximum real-time resolution of 10 µs. Output from
the digitizer can be displayed on an oscilloscope (Tektronix type 535
A), or plotted on an x-y plotter (Hewlett-Packard model 7044A) for a
hard copy.

Correlated experimental data are shown in Figures 14 to 18. Even
though pressures were measured at four axial locations, only the traces
at the entrance and the tip are shown in the figures. The first discern-
ible pressure rise for each pressure gauge occurred consecutively from
the crack entrance to the crack tip. The pressurization rates recorded
at various gauge locations along the crack indicate that the pressuriza-
tion rates decrease consecutively downstream of the crack entrance.
This attenuation can be attributed to the inert nature of the crack. A
typical pressure-time trace at the tip can be divided into three regions:
(1) the pressurization region where the pressure continuously increases;
(2) the constant pressure region; and (3) the depressurization region.
The uprising portion of the pressure-time trace at the crack tip loca-
tion is quite linear. In most of the tests, the ignition occurred
during the uprising portion of the pressure-time curve at the crack tip
location.

Ignition is defined in this report as the onset of emission of
luminous light from the propellant surface. This luminous light can be
detected by either the high-speed motion picture camera or the photo-
diode. The high-speed camera was used for all the tests; the photodiode
system was used only during the later tests. It was noted that the
photodiode system alone cannot give a very reliable signal (see Figure
18). This is due to the fact that the photodiode picks up light re-
flected from the walls of the stainless steel combustion chamber even
before the onset of ignition at the propellant tip. With a high-speed
motion picture it was possible to record a more complete ignition event,
thereby reducing the chance of error.

The common-time signal is not shown in any of the results presented
in Figures 14 to 18. This is because there is a 4 to 5 ms time lag
between the common-time signal and the first discernible pressure rise
at the pressure gauge located at the crack entrance. Since the region
of interest is the uprising portion of the pressure traces, that region
has been expanded, and, therefore, the common-time signal cannot be
included in the same figure. The time-correlated pressure and ignition
data indicated that the time of first discernible pressure rise coin-
cides with the appearance of hot igniter gases at the crack entrance.
The time delay between the appearance of the hot igniter gases at the
crack entrance and the ignition at the tip was obtained from the motion
picture recording. The time lag between the first discernible pressure
rises at the crack entrance and crack tip was obtained from the pres-
sure-time trace. The difference between these two time lags is the

43
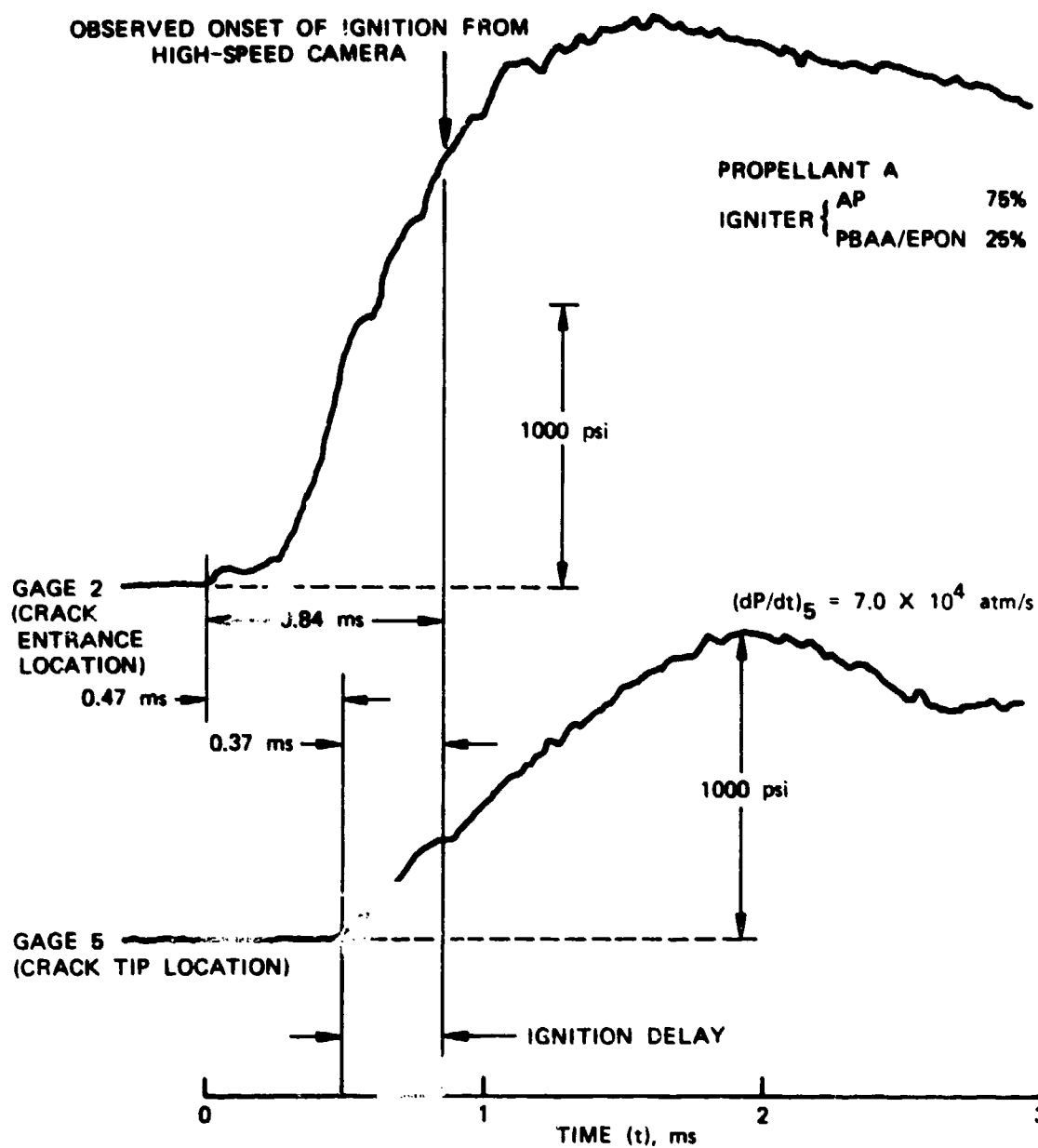
FIGURE 14. Measured Pressure-Time Traces for
Crack Tip Ignition Experiment (DNC Test No. 30).
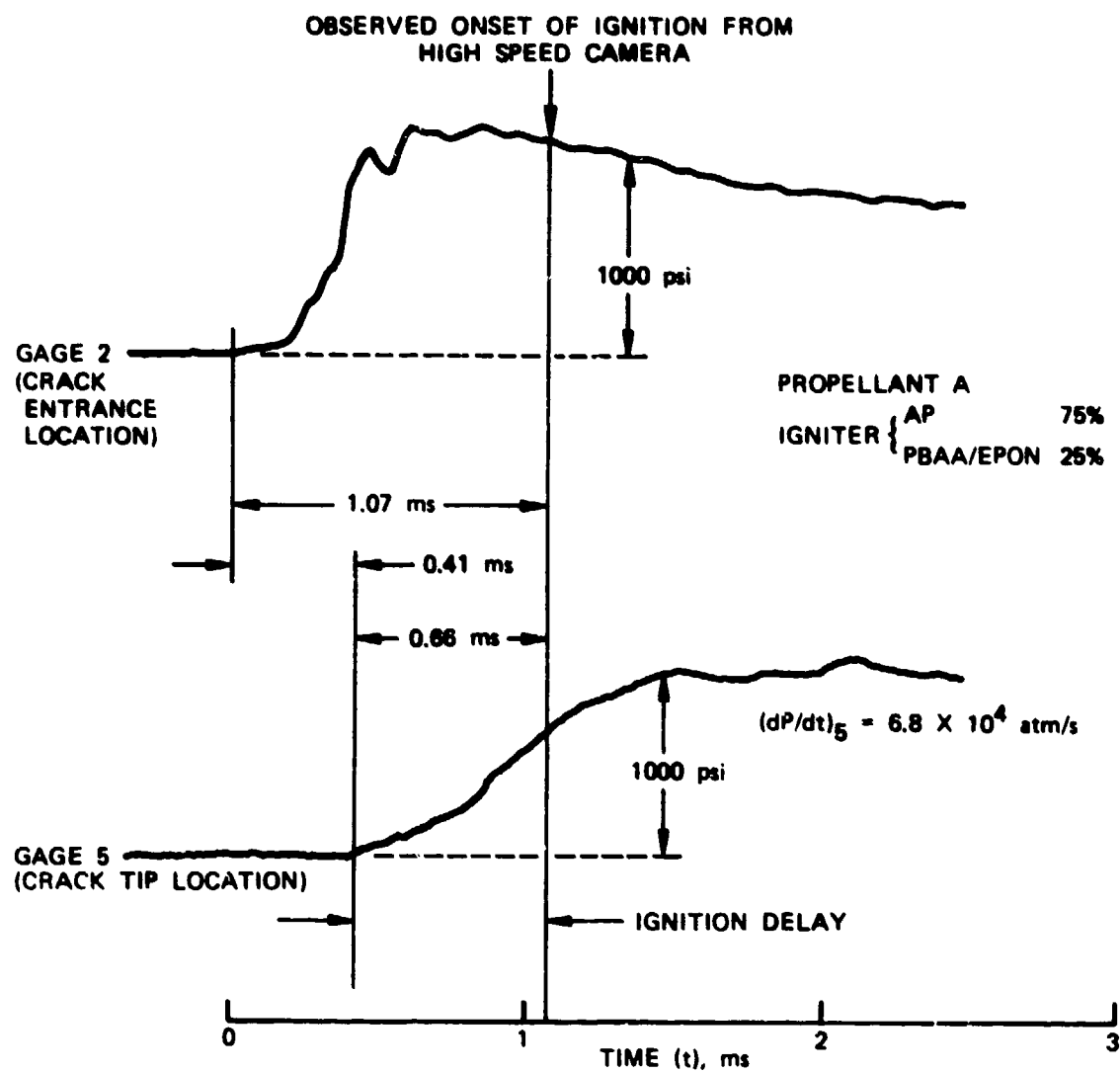
FIGURE 15. Measured Pressure-Time Traces for
Crack Tip Ignition Experiment (DNC Test No. 31).

45
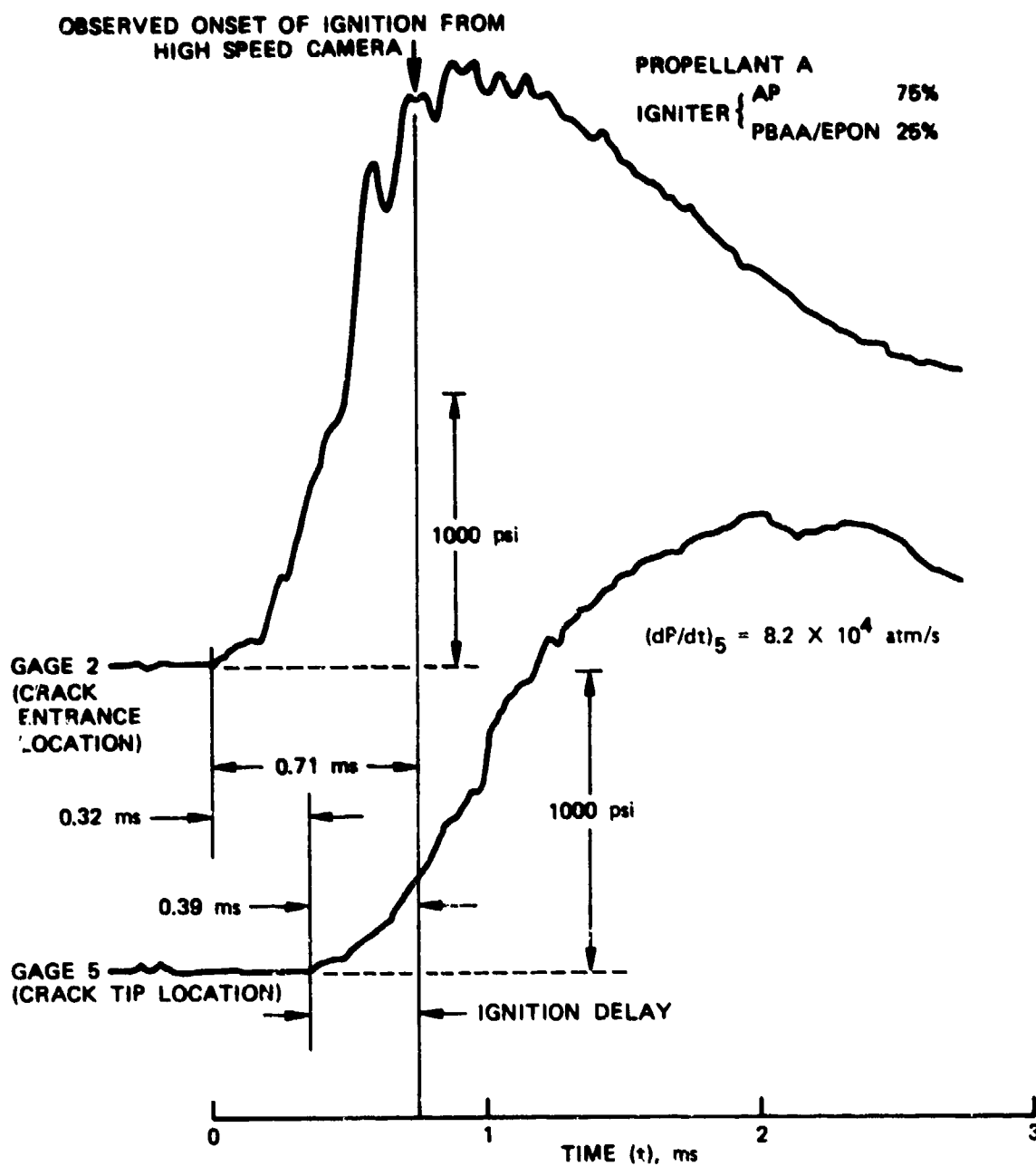
FIGURE 16. Measured Pressure-Time Traces for
Crack Tip Ignition Experiment (DNC Test No. 33).
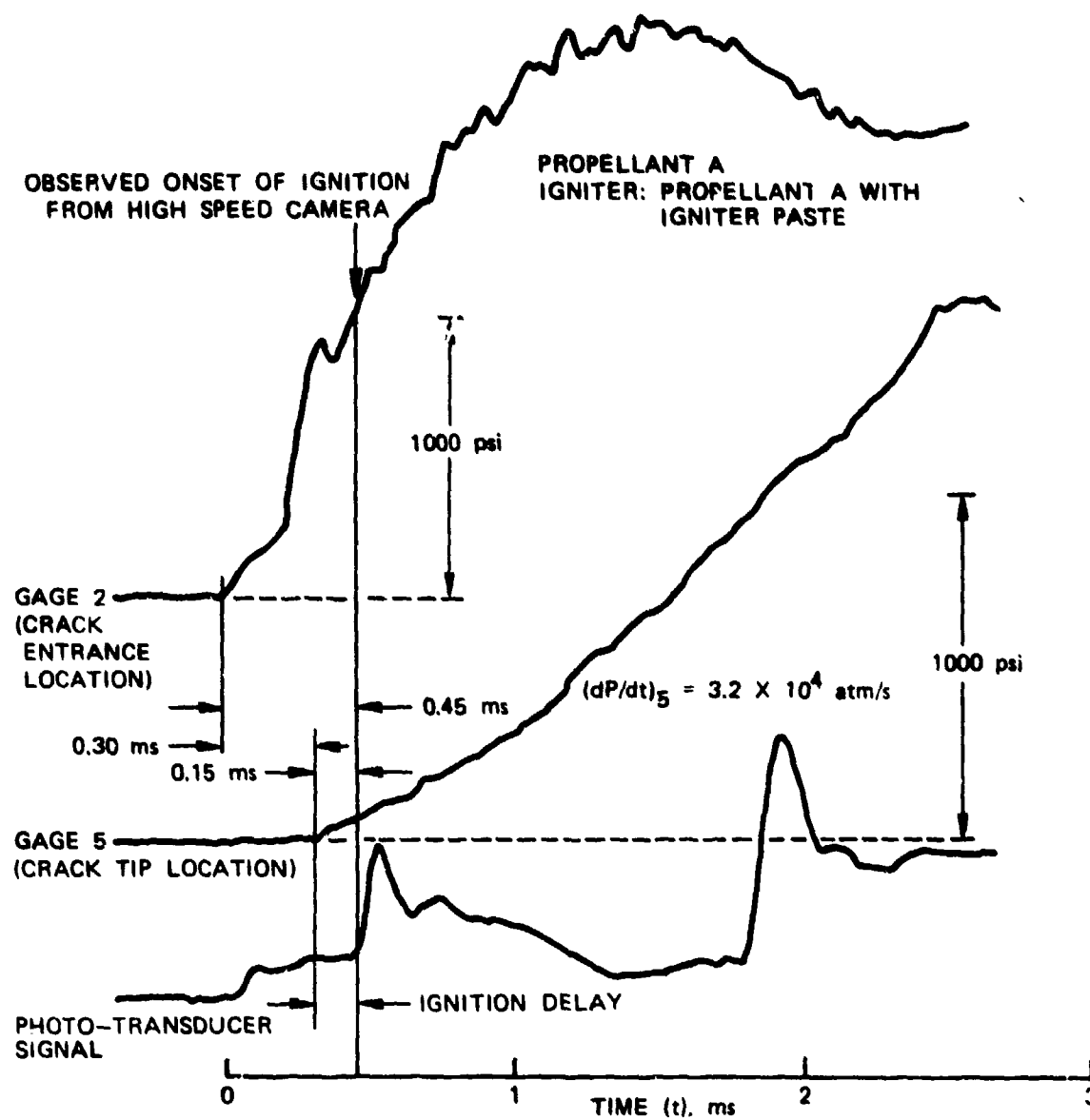
FIGURE 17. Measured Pressure-Time Traces for
Crack Tip Ignition Experiment (DNC Test No. 41).
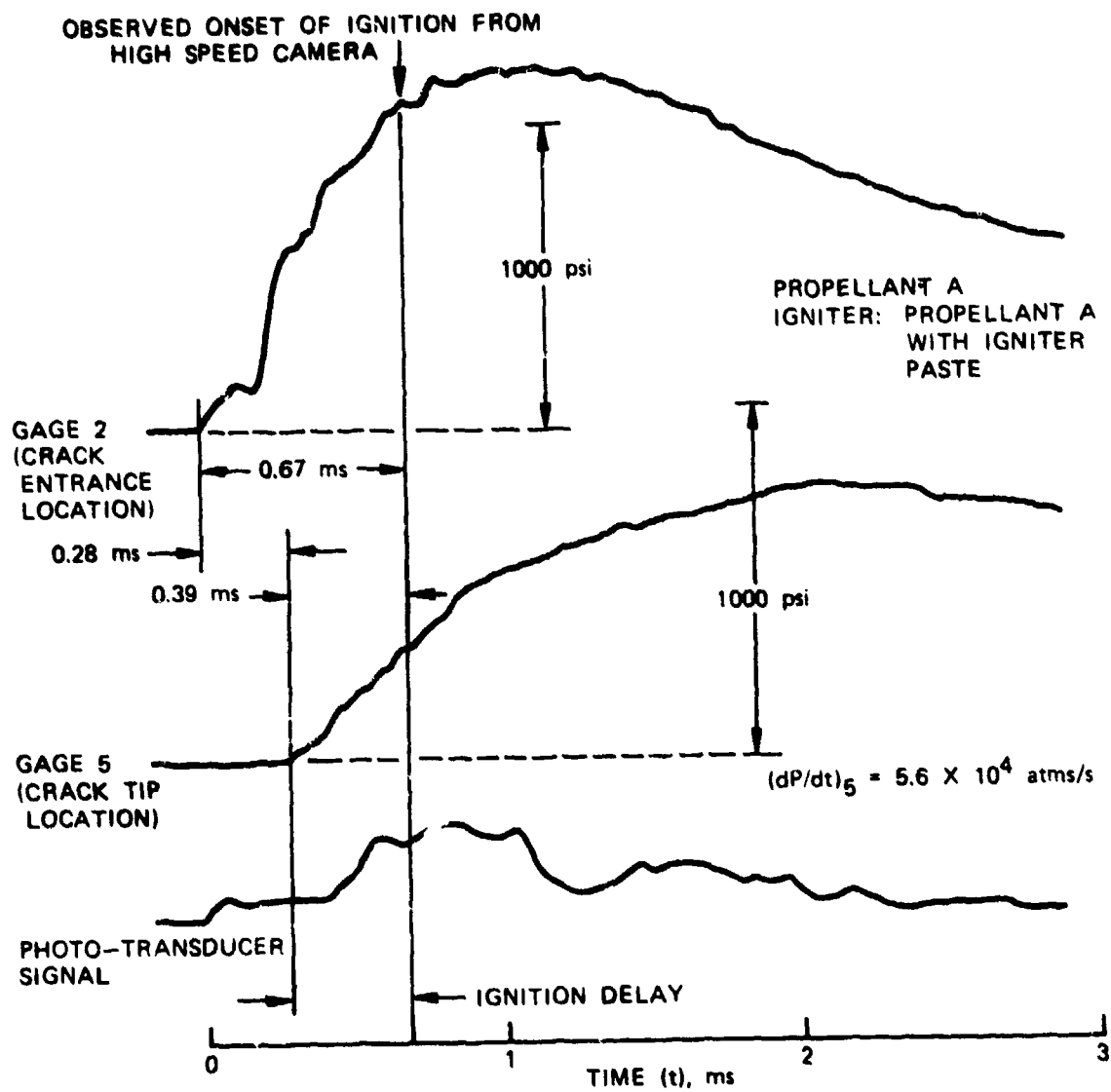
FIGURE 18. Measured Pressure-Time Traces for Crack Tip Ignition Experiment (DNC Test No. 42).

ignition delay time for the propellant at the tip. This is identical to the definition given in the section on Theoretical Work, i.e., the ignition delay time is the time lag between the arrival of the pressure wave at the tip and the incipient ignition. The plot of ignition delay time and pressurization rate is given in Figure 2 (Theoretical Work). Ignition delay times are plotted against the pressurization rate at the tip (Gage 5); no effort was made to relate them to pressurization rates at the crack entrance (Gage 2).

INVESTIGATION OF THE ONE-DIMENSIONALITY OF THE FLAME FRONT

Experimental firings were conducted to determine the one-dimensionality of the flame front. The crack was formed between a propellant slab which was slightly regressed below the brass leg assembly[1] and the inner surface of the plexiglass sacrificial window which was mounted on top of the leg assembly, i.e., one side of the crack was an inert, transparent, plexiglass window and the other side was the propellant slab. With this type of configuration, it was possible to observe the flame propagation process by looking directly at the burning propellant surface. A schematic diagram of the test sample used for this type of test is shown in Figure 19. The gap width of the crack was varied between 0.018 and 0.060 in. (0.46 and 1.52 mm). The length of the sample was about 7.2 in. (183 mm), and the width was about 0.7 in. (17.7 mm).

Two pressure traces were obtained for this configuration: one at the crack entrance and the other at the crack tip. The pressure traces for DNC Test No. 24 are shown in Figure 20. The two pressure traces are quite similar. The flame spreading event for DNC Test No. 24 is depicted in Figure 21. The filming rate approximately about 12,000 pictures per second. A detailed discussion of the flame spreading event is given in Table 2. Some of the general observations that can be made from these tests are: (1) the hot gases precede the ignition front along the crack and reach the tip much earlier than the convective ignition front; (2) the hot gases are luminous for a short time, with the luminosity disappearing later; this can be attributed to the quenching of the hot gases; (3) the flame front is nonuniform near the crack entrance, but becomes quite uniform along the crack and near the tip. It can be concluded that, except near the entrance region of the crack, the one-dimensional assumption for the flame propagation is quite appropriate. The nonuniformity of the flame front near the entrance region can be attributed to the nonuniform flow at the entrance of the rectangular-cross-sectional crack channel. These experiments support the one-dimensional assumption used in the theoretical model.
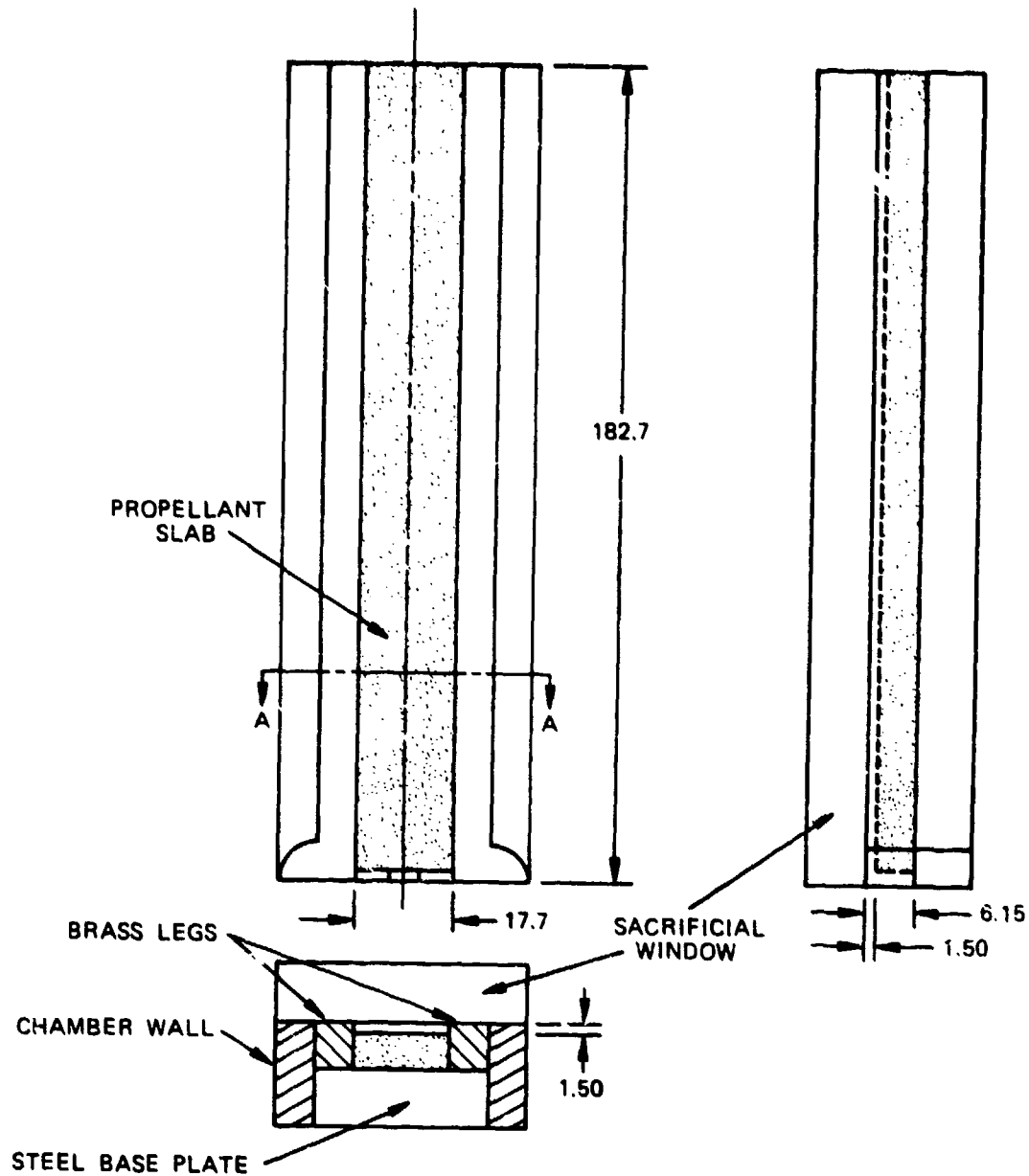
FIGURE 19. Geometric Configuration of the Propellant Sample Used in DNC Test No. 24. (All Dimensions are in mm)

IGNITER:
  FA-34 PRIMER
  PROPELLANT A CHARGE
    COATED WITH IGNITER
    PASTE, wt. = 2.067 g

G2
x = -0.345 cm

1000 psi

0

G5
x = 18.27 cm

SAMPLE:
  PROPELLANT A
  δ_{avg} = 0.15 cm
  L = 18.27 cm

1000 psi

0

TIME, ms

PICTURE NUMBER
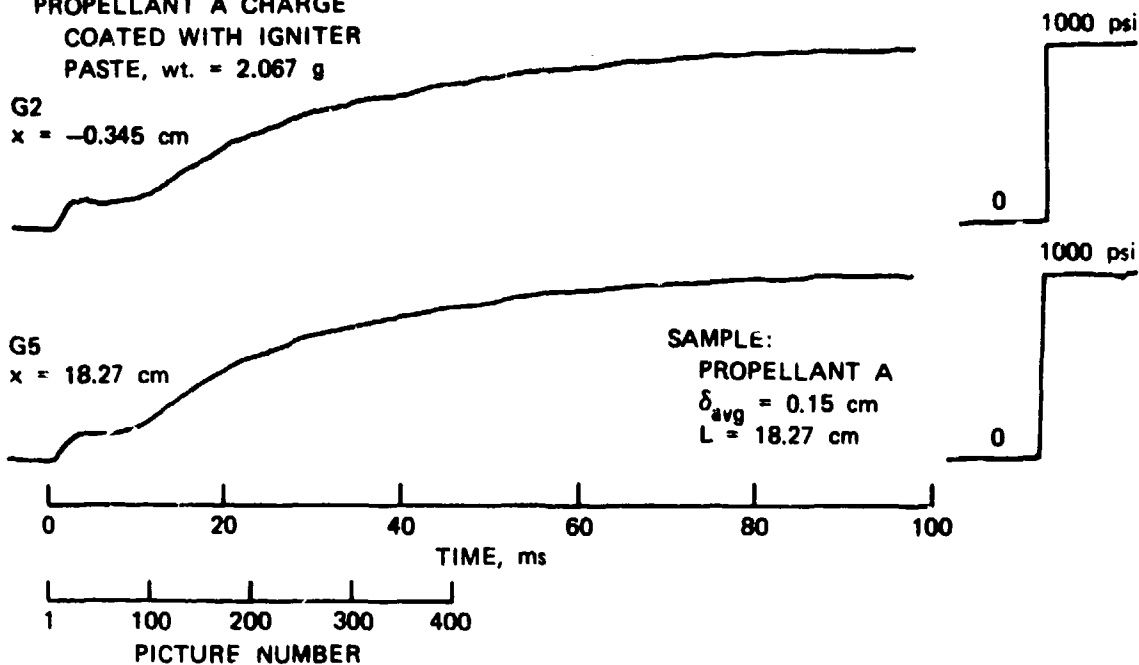
FIGURE 20. Expanded Short-Time Pressure
Traces of DNC Test No. 24.

EFFECT OF PROPELLANT CRACK GEOMETRY

Tests were continued for the purpose of studying the effect of
propellant crack geometry on the ignition and flame-spreading phenomena.
Since tests are still in progress, the detailed results and discussion
will be included in the next report. A millmount (an attachment to the
index table) has been designed and fabricated to manufacture tapered
cracks in the laboratory. Using the millmount, a maximum taper angle of
about 6 degrees can be manufactured. At very high chamber pressuriza-
tion rates, the present high-speed motion picture recording system gives
only a few useful pictures of the flame-spreading event. A quarter
frame head camera, capable of recording up to 44,000 pictures per second,
has been acquired through the Pennsylvania State University in order to
increase the number of pictures and to achieve better time resolution.
Even at this high speed, there is still the possibility that some events,
such as partial or transient ignition, etc., may not be filmed because
of the discrete nature of the framing process. At the suggestion of
Dr. R. L. Derr, a streak attachment to the Hycam camera was obtained to
alleviate this problem.

51

0 ms   0.91 ms   1.59 ms   2.15 ms

2.50 ms   2.61 ms   2.72 ms   2.84 ms
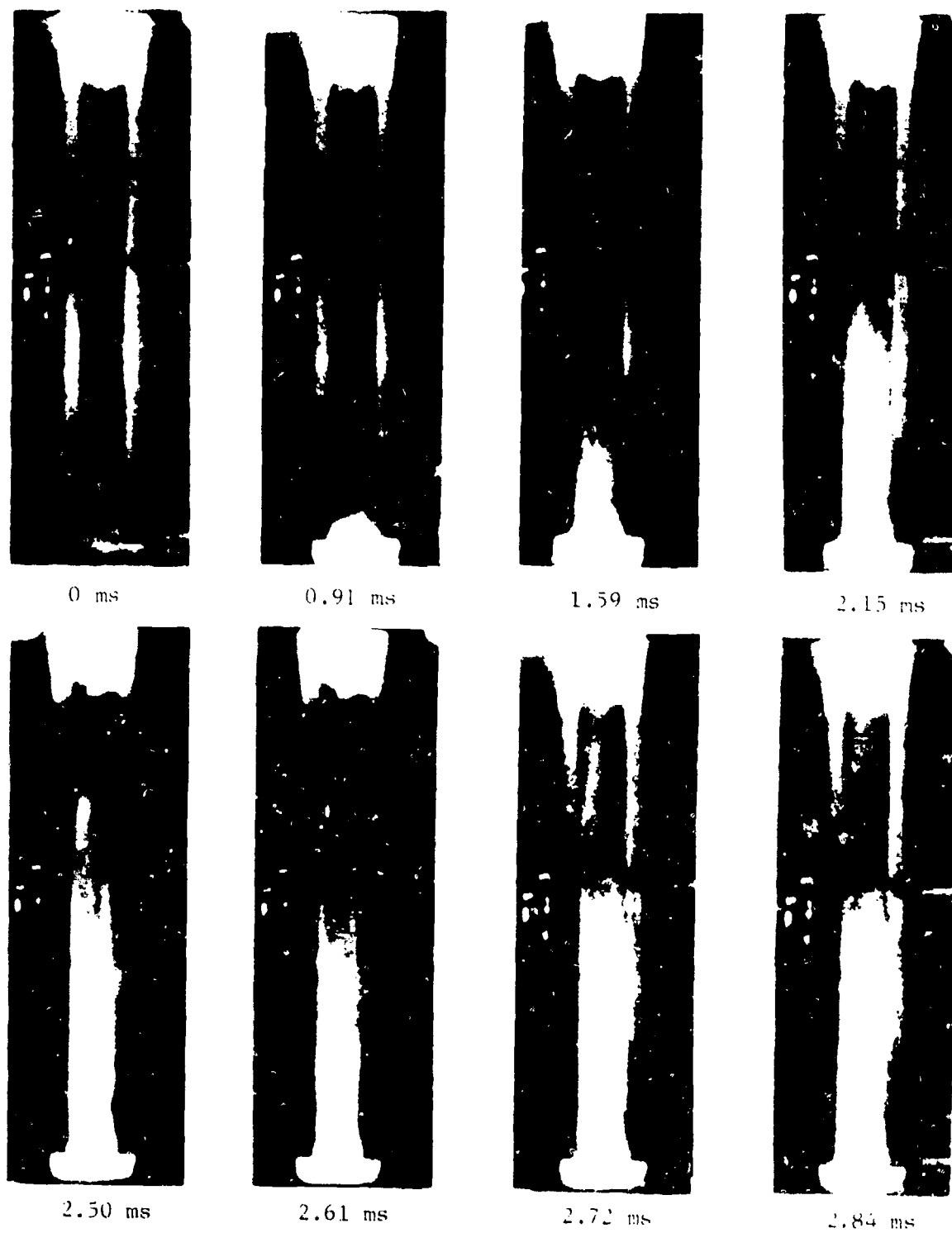
FIGURE 21. Motion Pictures of the Flame Spreading
Phenomenon for DNC Test No. 24.

| 3.06 ms | 4.42 ms | 5.67 ms | 6.69 ms |

| 9.00 ms | 10.32 ms |
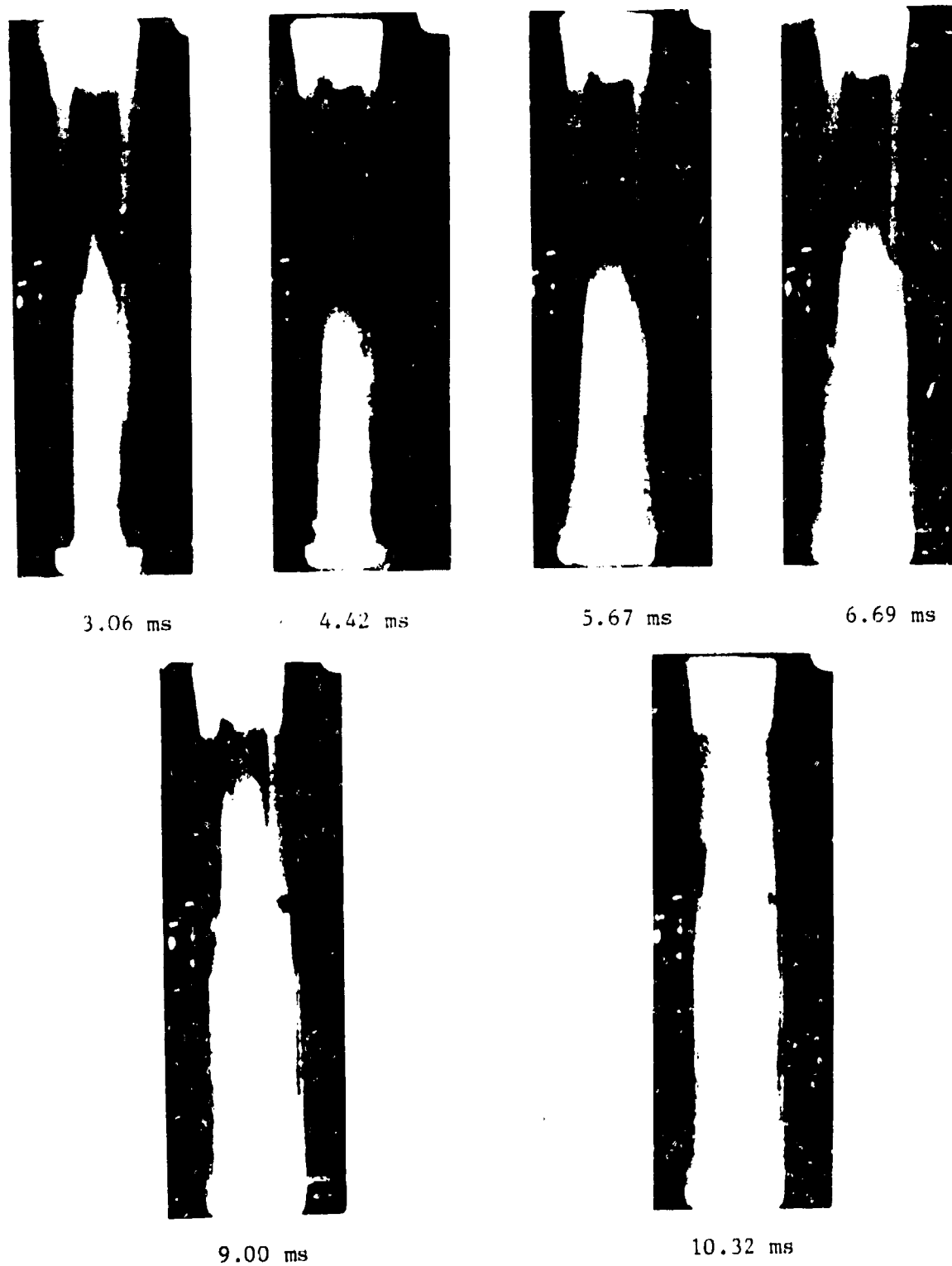
FIGURE 21. (Continued.)

53

TABLE 2. Interpretation of the Motion Pictures
in Figure 21 (DNC Test No. 24).

Picture No.	Time, ms	Observations and interpretations
1	0	Hot igniter gas enters the rectangular duct at the bottom of the main chamber
9	0.91	The crack entrance is ignited. Hot gases penetrate into the crack.
15	1.59	The ignition front is still near the entrance. The hot gases penetrate 30% of the crack.
20	2.15	The hot gases penetrate more than 30% of the crack.
23--25	2.50--2.72	Hot gases gradually penetrate the whole length of the crack. The ignition front still near the entrance region of the crack and appears nonuniform.
26	2.84	The luminosity of the hot gases starts to decrease.
28	3.06	The hot gas front recedes to about 70% of the crack. The ignition front moves up.
40	4.42	Hot gas front disappears. The ignition front penetrates about 50% of the crack length. Ignition front appears quite uniform.
50,60	5.67,6.69	The ignition front gradually moves up to about 66% of the crack. It appears quite uniform.
80,92	9.0,10.32	The ignition front eventually engulfs the whole crack length.

SUMMARY OF PROGRESS AND CONCLUSIONS

The progress made during the past 12 months in the study of combustion processes inside solid propellant cracks can be summarized as follows:

1. A theoretical model has been developed to explain the tip-ignition phenomena. It considers one-dimensional, unsteady mass and energy conservation equations for the gas-phase near the crack tip.

54

Experimentally observed pressure-time trace near the crack-tip region
has been used instead of a gas-phase momentum equation. A transient,
one-dimensional heat conduction equation is considered for the solid
phase.

2. A computer program has been implemented, based upon the above
theoretical model. It uses a stable, implicit scheme for the solution
of the finite-difference equations. The program can predict ignition
delay time, rate of heat flux to the propellant surface, temperature
distribution, etc., as functions of pressurization rates.

3. Experiments were conducted in an inert crack to eliminate some
of the possible mechanisms for the ignition at the tip. Test firings
were conducted in the inert crack to obtain the effect of pressurization
rate at the crack-tip on the ignition delay time of the test propellant
placed at the crack tip.

4. Both the theoretical and experimental results of the tip
ignition tests indicate that the ignition delay time decreases as the
pressurization rate is increased. Theoretically calculated ignition
delay times are in good agreement with experimental data. Based upon
this agreement, the ignition at the crack tip is considered to be caused
by the enhanced turbulent energy transport in the gas phase, which is
driven by strong compression waves.

5. The crack combustion code (CCC) has been merged with a struc-
tural analysis program (NFAP). Initial computer runs of the combined
code showed that the solid mechanics and combustion phenomena are inter-
dependent.

6. The crack geometry changes, not only because of burning, but
also because of mechanical deformation. The combustion phenomena could
either enhance or retard, depending upon the variation in geometry along
the crack. More realistic computation of the combustion phenomena
inside the crack should be based upon the combined program (CCC/NFAP).

7. The complete set of governing equations for describing the
transient combustion phenomena inside a solid propellant crack which
undergoes geometry change due to both combustion and mechanical deforma-
tion, has been nondimensionalized. A set of governing dimensionless
parameters has been obtained to aid future data correlation and analy-
sis.

8. Experiments were conducted to investigate the one-dimension-
ality of the ignition front. Results indicate that, except near the
entrance region of the solid propellant crack, the one-dimensional
assumption of the flame front propagation is quite appropriate.

9.   Experiments were continued to investigate the effect of pro-
pellant crack geometry on the ignition and flame-spreading phenomena. A
millmount has been designed and fabricated to manufacture tapered cracks.
A quarter frame head camera and a streak attachment to the high-speed
camera have been obtained to facilitate more accurate visual recording
of the flame-spreading and ignition events.

BIBLIOGRAPHY

Bathe, K. J., and E. L. Wilson. "NONSAP--A Nonlinear Structural Analysis Program," *Nuclear Engineering and Design*, Vol. 29, No. 2 (1974), pp. 266-293.

Chao, B. T. "End-Wall Heat Transfer in a Rarefaction Wave Tube," *J. Heat Transfer*, August 1965, pp. 349-352.

Favre, A. "Equations des Gaz Turbulents Compressibles," *J. de Mechanique*, Vol. 4, No. 3 (1965), pp. 361-390.

Fay, J. A., and N. H. Kemp. "Theory of Heat Transfer to a Shock-Tube End-Wall from an Ionized Monatomic Gas," *J. Fluid Mech.*, Vol. 21 (1965), pp. 659-672.

Hermance, C. E., R. Shinnar, and M. Summerfield. "Ignition of Hot, Stagnant Gas Containing an Oxidizer," *AIAA Journal*, Vol. 3, No. 9 (September 1965), pp. 1584-1592.

------. "Ignition of an Evaporating Fuel in a Hot Oxidizing Gas, Including the Effect of Heat Feedback," *Astronautica Acta*, Vol. 12, No. 2 (March-April 1966), pp. 95-112.

Kuo, K. K., A. T. Chen, and T. R. Davis. "Convective Burning in Solid-Propellant Cracks," *AIAA Journal*, Vol. 16, No. 6 (June 1978), pp. 600-607.

Levy, M. J., and J. H. Potter. "Some Transient Measurement in a Rarefaction Wave Tube," *J. of Engineering for Industry*, Translation ASME, Series B, Vol. 86 (November 1964), pp. 365-370.

McAlevy, R. F. "The Ignition Mechanism of Composite Solid Propellants," Ph.D. Thesis, Princeton University, June 1960.

McAlevy, R. F., P. L. Cowan, and M. Summerfield. "The Mechanism of Ignition of Composite Solid Propellants," *Solid Propellant Rocket Research*. Volume 1, Progress in Astronautics and Rocketry, an American Rocket Society series. New York, Adademic Press, 1960. Pp. 673-692.

Naval Weapons Center. *Transient Combustion in Solid Propellant Cracks*, by K. K. Kuo, D. R. McClure, A. T. Chen, and F. G. Lucas. China Lake, Calif., NWC, October 1977. (NWC TP 5943, publication UNCLASSIFIED.)

------. *Convective Burning in Isolated Solid Propellant Cracks*, by K. K. Kuo, R. L. Kovalcin, and S. J. Ackman. China Lake, Calif., NWC, February 1979. (NWC TP 6049, publication UNCLASSIFIED.)

Prachuktam, S., and T. Y. Chang. "NFAP--A Nonlinear Finite Element Analysis Program." University of Akron, Department of Civil Engineering, October 1976.

Appendix A

BASIC DEFINITIONS AND OPERATION RULE FOR FAVRE AVERAGING

Definitions

$$\rho = \overline{\rho} + \rho'$$

$$P = \overline{P} + P'$$

$$u = \widehat{u} + u''; \qquad T = \widetilde{T} + T''; \qquad h = \widetilde{h} + h''$$

Operation Rules

For any quantity, α,

$$\widetilde{\alpha} = \frac{\overline{\rho\alpha}}{\overline{\rho}}$$

$$\overline{\rho\alpha''} = 0$$

$$\overline{\alpha''} = -\frac{\overline{\rho'\alpha''}}{\overline{\rho}}$$

$$\overline{\alpha} - \widetilde{\alpha} = \overline{\alpha''}$$

$$\overline{\rho'\alpha''} = \overline{\rho'\alpha'}$$

$$\overline{\alpha''} = -\frac{\overline{\rho'\alpha'}}{\overline{\rho}}$$

Appendix B

DIFFICULTIES ENCOUNTERED IN OBTAINING ANALYTICAL SOLUTIONS

The final equation for the gas phase (Eq. 12) as derived in section 3 is:

$$\bar{\rho} \frac{\partial \bar{h}}{\partial t} - \left[\int_0^x \frac{\partial \bar{\rho}}{\partial t} \, dx \right] \frac{\partial \bar{h}}{\partial x} - \frac{\partial \bar{P}}{\partial t} = \frac{\partial}{\partial x} \left(k_{eff} \frac{\partial \bar{h}}{\partial x} \right) \tag{2-1}$$

If we make the following additional assumptions:

1. $\bar{P} = P_i (1 + ct^{\eta})$

2. $\bar{\rho} = \bar{\rho}_{\infty}$

3. Outside the thermal boundary layer near the propellant surface the compression process is iesentropic: i.e., $\dfrac{\bar{P}}{P_i} = \dfrac{T}{T_i}^{\frac{\gamma}{\gamma-1}} = (\dfrac{\bar{\rho}_{\infty}}{\rho_i})^{\gamma}$

4. $k = \dfrac{1}{2} [k_i + k_{\infty}]$

5. $k_{\infty} = k_i \left[\dfrac{T_{\infty}}{T_i} \right]^{\omega}$

Then Eq. (2-1) becomes:

$$\frac{\partial \hat{T}}{\partial t} - x \frac{\partial \hat{T}}{\partial x} \quad \frac{d}{dt} \ln \{ (1 + ct^{\eta})^{\frac{1}{\gamma}} \}$$

$$= T_i \frac{d}{dt} (1 + ct^{\eta})^{\frac{\gamma-1}{\gamma}}$$

$$+ \frac{\alpha_i}{2} \quad \frac{[1 + (1 + ct^{\eta})^{\frac{\gamma-1}{\gamma}\omega}]}{(1+ct^{\eta})^{1/\gamma}} \frac{\partial^2 T}{\partial x^2} \tag{2-2}$$

Introducing

$$\theta \equiv \frac{\hat{T}}{T_i} - (1 + ct^{\eta})^{\frac{\gamma-1}{\gamma}} \tag{2-3}$$

i.e., $\hat{T} = T_i [\theta + (1 + ct^{\eta})^{\frac{\gamma-1}{\gamma}}]$

$$\frac{\partial \hat{T}}{\partial t} = T_i [\frac{\partial \theta}{\partial t} + \frac{d}{dt} (1 + ct^{\eta})^{\frac{\gamma-1}{\gamma}}]$$

$$\frac{\partial \hat{T}}{\partial x} = T_i \frac{\partial \theta}{\partial x}$$

$$\frac{\partial^2 \hat{T}}{\partial x^2} = T_i \frac{\partial^2 \theta}{\partial x^2}$$

Substituting these into (2-2), we get:

$$\frac{\partial\theta}{\partial t} - x\frac{\partial\theta}{\partial x}\frac{d}{dt}\ln(1 + ct^\eta)^{\frac{1}{\gamma}} = \frac{\alpha_0}{2}\frac{[1 + (1+ct^\eta)^{\frac{\gamma-1}{\gamma}\omega}]}{(1 + ct^\eta)^{1/\gamma}}\frac{\partial^2\theta}{\partial x^2} \tag{2-4}$$

This equation can be transformed into the form of a diffusion equation by the following transformation:

$$\tau \equiv \frac{c^{\frac{1}{\eta}}}{2}\int_0^t [1 + (1 + ct^\eta)^{\frac{\gamma-1}{\gamma}\omega}](1 + ct^\eta)^{\frac{1}{\gamma}}dt \tag{2-5}$$

$$X \equiv xc^{\frac{1}{2\eta}}\alpha_0^{-\frac{1}{2}}(1 + ct^\eta)^{\frac{1}{\gamma}} \tag{2-6}$$

which results in:

$$\frac{\partial\theta}{\partial\tau} = \frac{\partial^2\theta}{\partial X^2} \tag{2-7}$$

I.c. $t = o \rightarrow \tau = o$: $\theta = o$

B.c.1 $x = o \rightarrow X = o$: $\theta = \theta_{ps}^{(\tau)}$ $\qquad$ (2-8)

B.c.2 $x \rightarrow -\infty$: $X \rightarrow -\infty$: $\theta \rightarrow o$

For the propellant, if we define

$$T_p \equiv T_p - T_i$$

Equation (1) of Section 3 becomes:

$$\frac{\partial^2 T_p}{\partial x^2} = \frac{1}{\alpha_p}\frac{\partial T_p}{\partial t} \tag{2-9}$$

I.c. $t = o$ $\qquad T_p = o$

B.c.1 $x = o$ $\qquad k_p\frac{\partial T_p}{\partial x} = k_{eff}T_i\frac{\partial\theta}{\partial X}c^{\frac{1}{2\eta}}\alpha_0^{-\frac{1}{2}}(1+ct^\eta)^{\frac{1}{\gamma}}\Big|_{X = o}$ $\qquad$ (2-10)

B.c.2 $x \rightarrow \infty$ $\qquad \theta = o$

In order to find a solution Eqs. (2-7) and (2-9) must be solved simultaneously.

A solution for Eq. (2-7) or (2-8) can be obtained using Duhamel's integral

theorem. However, when the heat flux is matched at the boundary (B.c.1 of

Eq. 2-10), one obtains an integral relationship, which does not seem to be

analytically solvable.

Appendix C

NFAP/CCC PROGRAM INPUT

Structural Analysis Input Format

I. **HEADING**

Card 1   (18A4)

Columns	Variable	Entry
1 - 72	HED(18)	Master heading information for use in labeling output

II. **MASTER CONTROL CARD**

Card 1   (I5, 6I1, I4, 13I5)

Columns	Variable	Entry
1 - 5	NUMNP	Total number of nodal points
6	IDOF(1)	Master X-translation code EQ.0: admissable EQ.1: deleted
7	IDOF(2)	Master Y-translation code
8	IDOF(3)	Master Z-translation code
9	IDOF(4)	Master X-rotation code
10	IDOF(5)	Master Y-rotation code
11	IDOF(6)	Master Z-rotation code
12 - 15	NEGL	Number of linear element groups EQ.0: all elements are nonlinear
16 - 20	NEGNL	Number of nonlinear element groups EQ.0: all elements are linear

Card 1 Continued

Columns	Variable	Entry
21 - 25	MODEX	Flag indicating solution mode EQ.0: data check and plot initial geometry EQ.1: execution EQ.2: restart
26 - 30	NSTEP	Number of solution time steps
31 - 35	IPRI	Output printing interval
36 - 40	ISAVE	Restart-save time step interval EQ.0: no saving for restart GE.1: interval of saving step
41 - 45	ISTAPE	Flag indicating saving solution on the tape EQ.0: no EQ.1: yes
46 - 50	IEQB	Specified block size EQ.0: calculated automatically during the program run
51 - 55	NRENUM	Flag indicating node renumbering to minimize bandwidth EQ.0: no node renumbering EQ.1: node renumbering
56 - 60	NPLOT	Flag indicating plotting option EQ.0: no plot EQ.1: plot initial mesh EQ.2: Plot geometry at selected time steps
61 - 65	NTIE	Tying degrees of freedom option EQ.0: not active EQ.1: active
76 - 80	ISTAT	Flag indicating static or dynamic analysis EQ.0: static analysis EQ.1: dynamic analysis

Card 2 (4I5, E10.4)

Columns	Variable	Entry
1 - 5	ISREF	Number of time steps between reforming effective stiffness matrix EQ.0: default set to 1
6 - 10	NUMREF	Number of allowable stiffness reformations in each time step
11 - 15	IEQUIT	Number of time steps between equilibrium iterations EQ.0: default set to 1
16 - 20	ITEMAX	Maximum number of equilibrium iterations EQ.0: default set to 15
21 - 30	RTOL	Relative tolerance used to measure equilibrium convergence EQ.0: default set to 10^{-3}

Card 3 (2F10.5)

Columns	Variable	Entry
1 - 10	TSTART	Time of solution start
11 - 20	DT	Time step increment

Card 4 (3I5, 2F10.2, 20X, 3F5.0)

Columns	Variable	Entry
1 - 5	KPLOT	Plotting option code to pick axis orientation
6 - 10	MAXND	Maximum number of nodes in any element to be plotted
11 - 15	MAXNM	Maximum number of elements in any group to be plotted
16 - 25	VLEN	Length of the horizontal axis

Card 4 Continued

Columns	Variable	Entry
26 - 35	WLEN	Length of the vertical axis
56 - 65	FAC	Scale factor to magnify displacements of deformed geometry
66 - 70	CMAG(1)	Scale factor to magnify X coordinates (including displacements)
71 - 75	CMAG(2)	Scale factor to magnify Y coordinates (including displacements)
76 - 80	CMAG(3)	Scale factor to magnify Z coordinates (including displacements)

Card 5 (15I5)

Columns	Variable	Entry
1 - 5	NPT(1)	First selected solution step to be plotted
6 - 10	NPT(2)	Second selected solution step to be plotted
---	----	------------
71 - 80	NPT(15)	15th selected solution step to be plotted

Card 6 (Blank)

control card to supress NFAP displacement printing routines

III. NODAL POINT DATA

Card 1   (A1, I4, A1, I4, 5I5, 3F10.0, I5)

(input as many cards as required for all nodes)

Columns	Variable	Entry
1	CT	Coordinate system code EQ.(blank): cartesian (X,Y,Z) EQ.X: X-cylindrical
2 - 5	N	Node (joint) number GE.1 and LE. NUMNP
6	PSF	Print suppression flag (ignored unless N.EQ.1) EQ.(blank): no suppression EQ.A: suppress list of nodal coord. EQ.B: suppress list of eqtn. numbers EQ.C: both A and B above
7 - 10	ID(1,N)	X-translation boundary code EQ.0: free EQ.1: fixed
11 - 15	ID(2,N)	Y-translation boundary code
16 - 20	ID(3,N)	Z-translation boundary code
21 - 25	ID(4,N)	X-rotation boundary code
26 - 30	ID(5,N)	Y-rotation boundary code
31 - 35	ID(6,N)	Z-rotation boundary code
36 - 45	X(N)	X coordinate
46 - 55	Y(N)	Y coordinate
56 - 65	Z(N)	Z coordinate
66 - 70	KN	Node number increment for nodal data generation EQ.0: no generation

IV. LOAD CONTROL CARDS

Card 1   (8I5)

Columns	Variable	Entry
1 - 5	NLOAD	Number of cards used to prescribe nodal forces
6 - 10	NLCUR	Total number of load curves (time functions)
11 - 15	NPTM	Maximum number of points used to describe one of the load curves GE. NLCUR
16 - 20	IMPACT	Impact loading EQ.0: no impact loading EQ.1: include impact loading
21 - 25	NPRES	Maximum number of elements in any element group subjected to pressure (no. of pressure subgroups)
26 - 30	NLCP	Number of load curves used for pressure load EQ.NLCUR
31 - 35	NDLS	Number of pressure load tables
36 - 40	IPGD	Pressure load with geometry dependent flag EQ.C: no EQ.1: yes

V. INITIAL CONDITIONS

Card 1 (Blank)

Insert blank to specify zero intial conditions

VI. TWO-DIMENSIONAL CONTINUUM ELEMENTS

Card 1   (3X, A1, 2I4, 4X, I4, 4X, I4, 8X, I4, 8X, I4, 4X, 4I4)

Columns	Variable	Entry
4	NPAR(1)	Enter "2" for 2-D elements
5 - 8	NPAR(2)	Number of 2-D elements in this group GE. 1
9 - 12	NPAR(3)	Type of nonlinear analysis EQ.0 or 1: material nonlinear analysis only EQ.2: total Lagrangian EQ.3: updated Lagrangian
17 - 20	NPAR(5)	Element type code EQ.0: axisymmetric EQ.1: plane strain EQ.2: plane stress
25 - 28	NPAR(7)	Maximum number of nodes to describe one element EQ.0: default set to 8
37 - 40	NPAR(10)	Numerical integration order to be used in Gauss quadrature formulae EQ.0: default set to 2 GE. 2 and LE. 4
49 - 52	NPAR(13)	Number of stress output location tables EQ.0: print stresses at integration points
57 - 60	NPAR(15)	Material model numbers EQ.1: linear isotropic EQ.9: linear viscoelastic
61 - 64	NPAR(16)	Number of different sets of material properties GE. 1
65 - 68	NPAR(17)	Number of constants per property set EQ.2: if NPAR(15) .EQ. 1 EQ.4: if(NPAR(15) .eq. 9
69 - 72	NPAR(18)	Dimension of storage array required for element history

Card 2   (I5)

Columns	Variable	Entry
1 - 5	N	Material property set number

Card 3A   (2F10.0)

Use if linear isotropic material

Columns	Variable	Entry
1 - 10	PROP(1,N)	Young's modulus
11 - 20	PROP(2,N)	Poisson's ratio

Card 3B   (4F10.0)

Use if linear viscoelastic material

Columns	Variable	Entry
1 - 10	PROP(1,N)	Bulk modulus
11 - 20	PROP(2,N)	G_∞ (first term in the relaxation modulus expression)
21 - 30	PROP(3,N)	$(G_0 - G_\infty)$, factor in the second term of the relaxation modulus expression
31 - 40	PROP(4,N)	Beta, exponential time constant in the relaxation modulus expression

Card 4A   (5I5)

Card 4A and 4B needed for each element

Columns	Variable	Entry
1 - 5	M	Element number GE. 1 and LE. NPAR(2)
6 - 10	IEL	Number of nodes used to describe this element EQ.0: default set to NPAR(7)

Card 4A Continued

Columns	Variable	Entry
11 - 15	IPS	Number of the stress table to be used in stress calculations EQ.0: no stress output for the element
16 - 20	MTYP	Material property set number assigned to this element GE. 1 and LE. NPAR(16)
21 - 25	KG	Node generation parameter used to compute node numbers for missing elements (given on the first card of the sequence) EQ.0: default set to 1

Card 4B   (8I5)

Columns	Variable	Entry
1 - 5	NOD(1)	Global node number of element node point 1
6 - 10	NOD(2)	Global node number of element node point 2
---	-----	------------------
36 - 40	NOD(8)	Global ncde number of element node point 8

VII. APPLIED LOADS

Card 1   (I5)

Columns	Variable	Entry
1 - 5	IPCCC	Code for pressure input source EQ.0: read pressure load from input deck EQ.1: Pressure load will be determined through linkage to the CCC program

Card 2A   (2I5)

Skip card set 2 if IPCCC .EQ. 1, otherwise supply
NLCUR sets with 2 or more cards per set

Columns	Variable	Entry
1 - 5	NTF	Time function number GE. 1 and LE. NLCUR
6 - 10	NPTS	Number of points used to describe this time function GE. 2 and LE. NPTM

Card 2B   (8F10.0)

Columns	Variable	Entry
1 - 10	TIMV(1)	Time at point 1, t_1
11 - 20	RV(1)	Function at point 1, t_1
21 - 30	TIMV(2)	Time at point 2, t_2
31 - 40	RV(2)	Function at point 2, t_2
---	-----	------------------
71 - 80	RV(4)	Function at point 4, t_4

(next card if required)

Columns	Variable	Entry
1 - 10	TIMV(5)	Time at point 5, t_5
11 - 20	RV(5)	Function at point 5, t_5
--	-----	------------------

Card 3A (3I5)

Repeat card set 3 NDLS times

Columns	Variable	Entry
1 - 5	N	Pressure table ID number
6 - 10	NFACE	Element face on which the pressure is acting
11 - 15	LTC	Load type code EQ.0: Default set to 1 EQ.1: normal pressure EQ.2: hydrostatic pressure

Card 3B (F10.0)

Columns	Variable	Entry
1 - 10	P(1)	Fraction of pressure at nodes along pressure loaded surface EQ. 1

Card 4 (2I5)

Columns	Variable	Entry
1 - 5	NG	Element group number
6 - 10	NPRSG	Number of subgroups of elements in this element group

Card 5   (5I5)

Repeat this card set for as many as NPRSG cards

Columns	Variable	Entry
1 – 5	NELPI	First element number for this subgroup
6 – 10	NELPF	Last element number for this subgroup
11 – 15	NELINC	Element number increment
16 – 20	ITABLE	Pressure table ID number
21 – 25	NCURP	Load curve ID number

Card 6   (Blank)

Place two blank cards at end of data to signal end of file

Convective Burning Analysis Input Format

I. HEADING

Card 1 (20A4)

Columns	Variable	Entry
1 - 80	TITLE(20)	Master heading information for use in labeling output

II. COMPUTATIONAL CONSTANTS

Card 1 (5E10.4)

Columns	Variable	Entry
1 - 10	XIP	Location of the inlet of the gap
11 - 20	XP	Distance downstream at which propellant begins
21 - 30	XG	Position at end of propellant in the crack
31 - 40	XE	Position at the end of the crack
41 - 50	BX	Body force

Card 2 (6E10.4)

Columns	Variable	Entry
1 - 10	W	Average molecular weight of all combustion gases
11 - 20	GAMA	Ratio of specific heats
21 - 30	ROPR	Density of solid propellant
31 - 40	FKPR	Thermal conductivity of solid propellant
41 - 50	ALPHAP	Thermal diffusivity of solid propellant
51 - 60	ROUGH	Equivalent relative roughness of the port wall

Card 3 (7E10.4)

Columns	Variable	Entry
1 - 10	TF	Adiabatic flame temperature
11 - 20	TPSCRI	Temperature at which surface ablation occurs
21 - 30	A	Pre-exponential factor in the non-erosive burning rate law
31 - 40	BREXP	Pressure exponent in the non-erosive burning rate law
41 - 50	EBC	Pre-exponential constant in the Lenoir-Robillard erosive burning relationship
51 - 60	EBEX	Factor in exponent of the Lenoir-Robillard erosive burning relationship
61 - 70	TPSIGN	Temperature at which ignition of the solid propellant occurs

Card 4 (4E10.4)

Columns	Variable	Entry
1 - 10	TGI	Initial gas temperature in the crack
11 - 20	PCI	Initial pressure in crack
21 - 30	UCI	Initial gas velocity in the crack (to facilitate the start of a numerical solution)
31 - 40	TPI	Initial propellant temperature

Card 5   (7I10)

Columns	Variable	Entry
1 - 10	NITER	Number of iterative predictor calculation EQ.1: the solution is obtained from quasilinearized inhomogeneous terms EQ.2: Predict twice before corrector calculation
11 - 20	NPRINT	Printing interval, number of time step calculations after which output is printed out GE. 1
21 - 30	NPUN	Output punching interval
31 - 40	NSPAVE	Number of time step calculations before space-averaging takes place
41 - 50	NBL	Number of time step calculations after each of which balance of the conservation and governing equation is performed and printed out
51 - 60	NINERT	Flag to indicate whether there is an inert wall or not EQ.0: no inert wall GT.0: inert wall present
61 - 70	NSLAB	Number of propellant slabs forming the crack EQ.1: there is one slab and one inert wall EQ.2: there are 2 propellant slabs forming the crack

Card 6   (3I10, 2E10.4)

Columns	Variable	Entry
1 - 10	NTPPDE	Flag to choose method of solution to find solid propellant temperature EQ.1: P.D.E. solution will be used to solve heat conduction equation NE.1: Goodman's integral solution will be used to solve surface temperature variation equation

Card 6   Continued

Columns	Variable	Entry
11 - 20	ISTART	Resart option code EQ.0: no restart NE.0: program restart
21 - 30	KXRITE	Node number at which the in-depth propellant temperature profile will be printed if NTPPDE EQ. 1. Print out occurs after every NBL time steps
31 - 40	FAC	Variable used to generate unequally spaced in-depth grid EQ.0: produces uniform grid EQ. 0.3 typically
41 - 50	YTPDIP	In-depth location where the dipstick ignition criterion applies

Card 7   (7E10.4)

Columns	Variable	Entry
1 - 10	DELTAX	Spacewise step for the numerical calculations
11 - 20	DELTAT	Time step for the numerical calculations
21 - 30	TI	Time of solution start
31 - 40	TMAX	Maximum time of a computer run or a restart run
41 - 50	EPSLON	Small value to bypass the singularity in the propellant surface temperature
51 - 60	DDRG	Friction coefficient multiplication factor
61 - 70	DDHC	Heat transfer coeeficient multiplication factor

Card 8   (4E10.4)

Columns	Variable	Entry
1 - 10	TSAV1	Time before which the space-averaging weight SAVMIN is used
11 - 20	TSAV2	Time after which the space-averaging weight SAVMAX is used
21 - 30	SAVMIN	Space-average percentage weight of the values at the neighboring mesh points specified for the time before TSAV1
31 - 40	SAVMAX	Space-average percentage weight of the values at the neighboring mesh points specified after TSAV2. Between TSAV1 and RSAV2 there is a linear increase in the space-average weight

Card 9   (4E10.4)

Columns	Variable	Entry
1 - 10	TTT1	Time before which the Crank-Nicolson parameter has the value THETAN
11 - 20	TTT2	Time after which the Crank-Nicolson parameter has the value THETAX
21 - 30	THETAN	Value of the Crank-Nicolson parameter for time before TTT1
31 - 40	THETAX	Value of tne Crank-Nicolson parameter for time after TTT2. Between TTT1 and TTT2, a linear increase is specified

III. GEOMETRY OF CRACK SAMPLE

Card 1   (I5)

Columns	Variable	Entry
1 - 5	NAPDVX	Number of points in the input table of crack geometry

Card 2   (3F15.6)

Supply NAPDVX sets of card 2

Columns	Variable	Entry
1 - 15	XAP	Distance from the entrance of the crack
16 - 30	BPD	Burning perimeter of the propellant crack
31 - 45	APD	Port area of the crack

Card 3   (3F15.6)

Supply NAPDVX sets of card 3

Columns	Variable	Entry
1 - 15	XAP	Distance from the entrance of the crack
16 - 30	WPD	Total wetted perimeter of the propellant crack
31 - 45	THETAG	Angle between propellant wall and the longitudinal axis of the crack

IV. TEST CONDITIONS

Card 1 (I5)

Columns	Variable	Entry
1 - 5	NTSTP	Number of points used to specify the chamber pressure and temperature of rocket with respect to time

Card 2 (3E12.4)

Supply NTSTP sets of card 2

Columns	Variable	Entry
1 - 12	PC	Chamber pressure of rocket
13 - 24	TC	Chamber temperature of rocket
25 - 36	TSTP	Time

Appendix D
SAMPLE DATA FOR NFAP/CCC COMBINED PROGRAM

NFAP INPUT DATA (INPUT UNIT 24)

```
CARD    1......10.......20.......30.......40.......50.......60.......70........80

  1     SAMPLE PROBLEM : 2/D ANALYSIS OF PROPELLANT CRACK (92 ELEMENTS)
  2     331100111 0   1   1 060   1     0     0     0     0     0     0     0
  3            1000
  4     0.0000075 0.0000075
  5            5   8  92                   8.0         4.0         5.0  1.0  3.0
  6            1   2   3   4   5   6   7   8   9  10  11  12  13  14  15
  7
  8            9           0   0                      0.00000  0.150
  9            8           0   0                      0.00000  0.200
 10           14           0   0                      0.48768  0.100          14
 11           23           0   0                      0.97536  0.050          14
 12          219           0   0                     14.63040  0.050          14
 13           28           0   0                      1.46304  0.050          14
 14          210           0   3                     14.14272  0.050          14
 15            7           0   0                      0.00000  0.250
 16          217           0   0                     14.63040  0.250          14
 17           13           0   0                      0.48768  0.250          14
 18          209           0   0                     14.14272  0.250          14
 19            5           0   0                      0.00000  0.450
 20          215           0   0                     14.63040  0.450          14
 21           12           0   0                      0.48768  0.450          14
 22          208           0   0                     14.14272  0.450          14
 23            3           0   0                      0.00000  0.650
 24          213           0   0                     14.63040  0.650          14
 25           11           0   0                      0.48768  0.650          14
 26          207           0   3                     14.14272  0.650          14
 27            1           1   1                      0.00000  0.850
 28          211           1   1                     14.63040  0.850          14
 29           10           1   1                      0.48768  0.850          14
 30          206           1   1                     14.14272  0.850          14
```

CARD	1....10	10	20	50	60	70
31	22	0	0	0.97536	0.150	14
32	218	0	0	14.63040	0.150	14
33	6	0	0	0.00000	0.350	
34	216	0	0	14.63040	0.350	14
35	4	0	0	0.00000	0.550	
36	214	0	0	14.63040	0.550	14
37	2	0	0	0.00000	0.750	
38	212	0	0	14.63040	0.750	
39	228	1	1	14.94790	0.850	26
40	306	1	1	16.85296	0.850	
41	237	1	1	15.26540	0.850	26
42	315	1	1	17.17040	0.850	
43	238	0	0	15.26540	0.750	26
44	290	0	0	16.53540	0.750	
45	229	0	0	14.94790	0.650	26
46	307	0	0	16.85290	0.650	
47	239	0	0	15.26540	0.650	26
48	291	0	0	16.53540	0.650	
49	240	0	0	15.26540	0.550	26
50	292	0	0	16.53540	0.550	
51	230	0	0	14.94790	0.550	26
52	308	0	0	16.85290	0.450	
53	241	0	0	15.26540	0.450	26
54	293	0	0	16.53540	0.450	
55	242	0	0	15.26540	0.350	26
56	294	0	0	16.53540	0.350	
57	231	0	0	14.94790	0.250	26
58	305	0	0	16.85290	0.250	
59	243	0	0	15.26540	0.250	26
60	295	0	0	16.53540	0.250	

CARD	1......10......20......30......40......50......60......70......80					
61	244	0	0	15.26540	0.150	26
62	296	0	0	16.53540	0.150	
63	232	0	0	14.94790	0.050	26
64	310	0	0	16.85290	0.050	
65	245	0	0	15.26540	0.050	26
66	297	1	0	16.53540	0.050	
67	316	1	1	17.17040	0.750	
68	317	1	1	17.17040	0.650	
69	318	1	1	17.17040	0.550	
70	319	1	1	17.17040	0.450	
71	320	1	1	17.17040	0.350	
72	321	1	1	17.17040	0.250	
73	322	1	1	17.17040	0.150	
74	323	1	1	17.17040	0.050	
75	220	0	0	14.63040	0.04375	26
76	298	0	0	16.53540	0.04375	
77	221	0	0	14.63040	0.03750	26
78	299	0	0	16.53540	0.03750	
79	233	0	0	14.94790	0.03750	26
80	311	0	0	16.85290	0.03750	
81	222	0	0	14.63040	0.03125	26
82	300	0	0	16.53540	0.03125	
83	223	0	0	14.63040	0.02500	26
84	301	0	0	16.53540	0.02500	
85	234	0	0	14.94790	0.02500	26
86	312	0	0	16.85290	0.02500	
87	224	0	0	14.63040	0.01875	26
88	302	0	0	16.53540	0.01875	
89	225	0	0	14.63040	0.01250	26
90	303	0	0	16.53540	0.01250	

CARD	1....10	16	20	30	40	50	60	70
91	235	0	0			14.94790	0.01250	26
92	313	0	0			16.85290	0.01250	26
93	226	0	0			14.63040	0.00625	
94	304	0	0			16.53540	0.00625	
95	227	0	1			14.63040	0.00000	
96	236	0	1			14.94790	0.00000	
97	253	0	1			15.26540	0.00000	
98	262	0	1			15.58290	0.00000	
99	279	0	1			15.90040	0.00000	
100	288	0	1			16.21790	0.00000	
101	305	0	1			16.53540	0.00000	
102	314	0	1			16.85290	0.00000	
103	324	1	1			17.17040	0.04375	
104	325	1	1			17.17040	0.03750	
105	326	1	1			17.17040	0.03125	
106	327	1	1			17.17040	0.02500	
107	328	1	1			17.17040	0.01875	
108	329	1	1			17.17040	0.01250	
109	330	1	1			17.17040	0.00625	
110	331	1	1			17.17040	0.00000	
111	0	16	0	16	1	0	0	
112								
113	2 92	3	1	23	16	2	1	1 4 16
114	1			8	0	0		
115	49201429.	14901.		45969.	0.095			
116	1	0	1	14	1			
117	3	17 15	1	11 16	10	2		
118	15 8	0	1		2			
119	199 213	211	197	207 212	206 198			
120	16 8	0		26				

```
                1......10........20........30........40........50........60........70........80
```

CARD								
121	213	239	237	211	229	238	228	212
122	19	8	0	1				
123	291	317	315	289	307	316	306	290
124	20	8	0	1				
125	5	19	17	3	14	18	11	4
126	34	8	0	1				
127	201	215	213	199	208	214	207	200
128	35	8	0	1	26			
129	215	241	239	213	230	240	229	214
130	38	8	0	1				
131	293	319	317	291	308	318	307	292
132	39	8	0	1	14	20	12	6
133	7	21	19	5	13			
134	53	8	0	1				
135	203	217	215	201	209	216	208	202
136	54	8	0	1	26			
137	217	243	241	215	231	242	230	216
138	57	8	0	1				
139	295	321	319	293	309	320	308	294
140	58	8	0	1	14	22	13	8
141	9	23	21	7	14			
142	72	8	0	1				
143	205	219	217	203	210	218	209	204
144	73	8	0	1	26			
145	219	245	243	217	232	244	231	218
146	76	8	0	1				
147	297	323	321	295	310	322	309	296
148	77	8	0	1	26			
149	221	247	245	219	233	246	232	220
150	80	8	0	1				

```
CARD    1.......10........20........30........40........50........60........70........80

151     299   325   323   297   311   324   310   298
152      81     8     0     1    26
153     223   249   247   221   234   248   233   222
154      84     8     0     1
155     301   327   325   299   312   326   311   300
156      85     8     0     1    26
157     225   251   249   223   235   250   234   224
158      88     8     0     1
159     303   329   327   301   313   328   312   302
160      89     8     0     1    26
161     227   253   251   225   236   252   235   226
162      92     8     0     1
163     305   331   329   303   314   330   313   304
164       1     1     1           1
165       1     1
166     1.0
167       2     4     1           1
168     1.0
169       1    23     1     1
170      58    58     1     1
171      59    59     1     1     2
172      60    60     1     1     3
173      61    61     1     1     4
174      62    62     1     1     5
175      63    63     1     1     6
176      64    64     1     1     7
177      65    65     1     1     8
178      66    66     1     1     9
179      67    67     1     1    10
180      68    68     1     1    11
```

91

CARD	1......10		20		
181	69	69	1	1	12
182	70	70	1	1	13
183	71	71	1	1	14
184	72	72	1	1	15
185	77	77	1	2	15
186	81	81	1	2	15
187	85	85	1	2	15
188	89	89	1	2	15
189	1	1	1	2	16
190	20	20	1	2	16
191	39	39	1	2	16
192	58	58	1	2	16
193					
194					

30........40........50........60........70........80

CCC INPUT DATA (INPUT UNIT 50)

```
CARD    1.......10.......20.......30.......40.......50.......60.......70.......80
  1     #DNC NO.21 INITIAL INPUT AT TIME ZERO (NEW)
  2     0.0000E 001.0000E-021.4610E 011.4630E 010.5000E 001.0000E 00
  3     2.6100E 011.2100E 001.7100E 008.0000E-041.8090E-032.5000E-02
  4     3.0000E 038.6000E 029.3590E-034.1080E-010.7000E 000.5300E 020.9200E 03
  5     2.9850E 021.0334E 031.0000E 012.9820E 02
  6          1    015    4000    1    4000    1    2
  7          0    0    20.2000D-000.0000D-00
  8     4.8767E-010.5000E-060.0000E 002.5000E-031.0000E-012.0000E 00
  9     1.0000E-022.0000E-023.0000E-028.0000E-02
 10     1.0000E-022.0000E-026.0000E-016.0000E-01
 11          4
 12     0.0           5.08      0.762000
 13     0.48767       5.08      0.508000
 14     0.97534       5.08      0.254000
 15     14.63         5.08      0.254000
 16     0.0000        5.6800    0.0
 17     0.48757       5.4800    0.0
 18     0.97534       5.2800    0.0
 19     14.63         5.2800    0.0
 20          5
 21     10.33500E 0218.000000E 02 0.000000E 00
 22     20.66460E 0222.000000E 02 0.00200E-03
 23     30.99690E 0226.000000E 02 0.00400E-03
 24     41.32920E 0230.000000E 02 0.00600E-03
 25     15.50878E 0530.000000E 02 3.00000E-03
```

NOMENCLATURE

A	Axial transformation constant for the gaseous region, cm^{-1}
Al	Axial transformation constant for the solid region, cm^{-1}
A_p	Cross-sectional area of the crack, cm^2
c_p	Specific heat at constant pressure, $cal/g-K$
e	Strain deviator
g	Acceleration of gravity, conversion factor, $g-cm/g_f-s^2$
G_1	Relaxation Modulus, g_f/cm^2
$\bar{h}$	Enthalpy of gas, cal/g
$\bar{h}_c$	Local convective heat transfer coefficient, cal/cm^2-s-K
L	Length of the crack, cm
k	Thermal conductivity $cal/cm-s-K$
k_{eff}	$k + k_t$
K	Bulk modulus, g_f/cm^2
M_w	Molecular weight, $g_f/g-mole$
P	Pressure, g_f/cm^2
Pr	Prandtl number
p	Pressure, g_f/cm^2
$\mathscr{P}_b$	Burning perimeter, cm
$\mathscr{P}_w$	Wetted perimeter of the port, cm
R	Specific gas constant for the combustion gases, $g_f-cm/g-K$
Re	Reynolds number
T	Temperature (without subscript, gas temperature), K
T_f	Adiabatic flame temperature of the solid propellant, K
T_{pi}	Initial propellant temperature, K
T_{ps}	Propellant surface temperature, K
t	Time, s
u	Gas velocity, cm/s
x	Axial coordinate, measured from propellant surface, cm
z	Transformed nondimensional axial coordinate
α	Thermal diffusivity, cm^2/s
β	Time constant, s^{-1}
γ	Ratio of specific heats
δ	Gap width of the crack, cm
ε	Strain tensor
λ	Thermal conductivity, $cal/cm-s-K$
μ	Gas viscosity, $g/cm-s$

ρ Density (without subscript, gas density), g/cm^3

σ Stress tensor

ϕ Dissipation, cal/cm^3-s

Subscripts

c   Rocket chamber

cri   Critical condition for surface ablation

fp   Flame propagation

i   Initial value

ign   Ignition condition

p, pr   Propellant

t   Turbulent

Superscripts

~   Dimensionless parameters or Favre averaged quantity

*   Reference parameters

—   Reynold's or time averaged quantity

'   Fluctuating quantities in Reynold's average method

"   Fluctuating quantities in Favre's average method

INITIAL DISTRIBUTION

1 Assistant Deputy Chief of Naval Material for Laboratory
  Management
8 Naval Air Systems Command
    AIR-00D4 (2)
    AIR-30212 (2)
    AIR-320 (1)
    AIR-330B, Robert Brown (1)
    AIR-330D (1)
    AIR-536 (1)
4 Chief of Naval Operations
2 Chief of Naval Material
    MAT-07 (1)
    MAT-08 (1)
6 Naval Sea Systems Command
    SEA-003 (1)
    SEA-62R2
      Cassel (1)
      Murrin (1)
    SEA-9961 (1)
    SEA-99612 (2)
7 Chief of Naval Research, Arlington
    ONR-100 (1)
    ONR-102 (1)
    ONR-400 (1)
    ONR-420 (1)
    ONR-472 (1)
    ONR-473
      Richard Miller (1)
      James R. Patton, Jr. (1)
2 Naval Ordnance Station, Indian Head
    Code 525, Peter Stang (1)
    Technical Library (1)
3 Naval Postgraduate School, Monterey
    Code 57, Fuhs (1)
    Code 57NT, Netzer (1)
    Technical Library (1)
3 Naval Research Laboratory
    Code 2021 (1)
    Code 6130, Chemistry Division (1)
    Technical Library (1)

2 Naval Surface Weapons Center Detachment, White Oak
  Laboratory, Silver Spring
    Code 240, Sigmund Jacobs (1)
    G. B. Wilmot (1)
1 Naval Underwater Systems Center, Newport (Code 5B331, Robert S. Lazar)
1 Naval Weapons Evaluation Facility, Kirtland Air Force Base (Code 401)
2 Navy Strategic Systems Project Office
    SP-2731, Roy Kinert (1)
    NSP-2731, Throckmorton (1)
2 Army Armament Research and Development Command, Dover
    (DRDAR-SCA-PE, L. Stiefel (1)
    LCWSL, C. Lenchitz (1)
1 Army Missile Command, Redstone Scientific Information
  Center, Redstone Arsenal (DRDMI-RK, Dr. R. G. Rhoades)
1 Army Armament Research & Development Command, Dover
  (DRDAR-LCE, J. Picard)
3 Army Ballistic Research Laboratories, Aberdeen Proving Ground
    DRDAR-BLP
      Austin W. Barrows (1)
      Ingo W. May (1)
    DRDAR-TSB-S (STINFO) (1)
1 Rock Island Arsenal (Edward Haug)
1 Air Force Armament Laboratory, Eglin Air Force Base (DLDL,
  Otto K. Heiney)
3 Air Force Rocket Propulsion Laboratory, Edwards Air Force Base
    DYSC, Wilbur C. Andrepont (1)
    Robert Geisler (1)
    Dr. R. Weiss (1)
2 Air Force Office of Scientific Research
    Leonard Caveny (1)
    Bernard T. Wolfson (1)
12 Defense Technical Information Center
1 National Aeronautics & Space Administration (Code RP,
  Frank W. Stephenson, Jr.)
2 George C. Marshall Space Flight Center
    SE-ASTN-PEA, John Q. Miller (1)
    Richard J. Richmond (1)
1 Lewis Research Center (Richard J. Priem)
1 Lyndon B. Johnson Space Center (EP, Joseph G. Thibodaux)
1 Aerojet Solid Propulsion Company, Sacramento, CA (Dept 4350,
  M. Ditore) via AFPRO
1 Aeronautical Research Associates of Princeton, Inc., Princeton,
  NJ (R. A. Reddini)
1 Aerospace Corporation, Los Angeles, CA (Ellis M. Landsbaum)
1 Allegany Ballistics Laboratory, Cumberland, MD (Roy R. Miller)
1 Atlantic Research Corporation, Alexandria, VA (Merrill K. King)
1 Battelle Memorial Institute, Columbus, OH (Abbott A. Putman)
1 Brigham Young University, Provo, UT (673/W1dB, M. Beckstead)
1 California State University Sacramento, Sacramento, CA
  (School of Engineering, Frederick H. Reardon)

1 Calspan Corporation, Buffalo, NY (Edward B. Fisher)
1 Chemical Propulsion Information Agency, Applied Physics Laboratory,
  Laurel, MD (Thomas W. Christian)
3 Georgia Institute of Technology, Atlanta, GA
    Ben T. Zinn (1)
    Edward W. Price (1)
    Warren C. Strahle (1)
1 General Applied Science Laboratory, Westbury Long Island, NY
  (John Erdos)
1 General Dynamics Corporation, Pomona Division, Pomona, CA
  (Paul L. Boettcher)
2 Hercules Incorporated, Bacchus Works, Magna, UT
    Ken McCarty (1)
    Ronald L. Simmons (1)
1 Hercules, Incorporated, McGregor, TX (William G. Haymes)
1 Institute for Defense Analyses, Arlington, VA (R. C. Oliver)
2 Jet Propulsion Laboratory, Pasadena, CA
    Fred E. C. Culick (1)
    Leon D. Strand (1)
2 Lockheed Missiles and Space Company, Sunnyvale, CA
    J. Linsk (1)
3 Lockheed Palo Alto Research Laboratory
    R Byrd (1)
    G. Lo (1)
    H. Marshall (1)
26 Pennsylvania State University
    Applied Research Lab., Gerard M. Faeth (1), Kenneth K. Kuo (25)
1 Princeton Combustion Research Laboratories, Princeton, NJ
  (M. Summerfield)
1 Purdue University, West Lafayette, IN (School of Mechanical
  Engineering, John R. Osborn)
1 Rockwell International Corporatio , Canoga Park, CA (BA08, Joseph
  E. Flanagan)
1 Science Applications, Inc., Woodland Hills, CA (R. B. Edelman,Suite 243)
1 Southwest Research Institute, San Antonio, TX (Fire Research
  Section, William H. McLain)
1 TRW Systems, Inc., Redondo Beach, CA (A. C. Ellings)
1 Thiokol Corporation, Huntsville Division, Huntsville, AL
  (David A. Flanigan)
1 Thiokol Corporation, Wasatch Division, Brigham City, UT
1 United Technologies Corporation, East Hartford, CT (R. H. W. Waesche)
1 United Technologies Corporation, Sunnyvale, CA (Chemical
  Systems Division, Robert S. Brown)
1 Universal Propulsion Company, Ind., Phoenix, AZ
1 University of California, San Diego, La Jolla, CA (AMES Dept,
  Forman A. Williams)
1 University of Illinois, Urbana, IL (AAE Dept., Herman Krier)
1 University of Southern California, Los Angeles, CA (Mechanical
  Engineering Dept/OHE230, M. Gerstein)

2 University of Utah, Salt Lake City, UT
    Dept of Chemical Engineering, Alva D. Baer (1)
    G. A. Flandro (1)
2 Whittaker Corporation, Bermite Division, Saugus, CA
    L. Bloom (1)
    L. LoFiego (1)
1 University of Waterloo, Ontario, Canada (Department of Mechanical
    Engineering, Clarke E. Hermance) via Naval Air Systems Command
    (AIR-960)